ORIGINAL ARTICLE

Exosomes derived from pulmonary metastatic sites enhance osteosarcoma lung metastasis by transferring the miR-194/215 cluster targeting MARCKS

Pei Yu, Yubao Han, Lulu Meng, Yanyuan Tian, Zhiwei Jin, Jun Luo, Chao Han, Wenjun Xu, Lingyi Kong*, Chao Zhang*

State Key Laboratory of Natural Medicines, Jiangsu Key Laboratory of Bioactive Natural Product Research, School of Traditional Chinese Pharmacy, China Pharmaceutical University, Nanjing 211198, China

Abstract Osteosarcoma, a prevalent primary malignant bone tumor, often presents with lung metastases, severely impacting patient survival rates. Extracellular vesicles, particularly exosomes, play a pivotal role in the formation and progression of osteosarcoma-related pulmonary lesions. However, the communication between primary osteosarcoma and exosome-mediated pulmonary lesions remains obscure, with the potential impact of pulmonary metastatic foci on osteosarcoma progression largely unknown. This study unveils an innovative mechanism by which exosomes originating from osteosarcoma pulmonary metastatic sites transport the miR-194/215 cluster to the primary tumor site. This transportation enhances lung metastatic capability by downregulating myristoylated alanine-rich C-kinase substrate (MARCKS) expression. Addressing this phenomenon, in this study we employ cationic bovine serum albumin (CBSA) to form nanoparticles (CBSA-anta-194/215) *via* electrostatic interaction with antagomir-miR-194/215. These nanoparticles are loaded into nucleic acid-depleted exosomal membrane vesicles (anta-194/215@Exo) targeting osteosarcoma lung metastatic sites. Intervention with bioengineered exosome mimetics (anta-194/215@Exo) not only impedes osteosarcoma progression but also significantly prolongs the lifespan of tumor-bearing mice. These findings suggest that pulmonary metastatic foci-derived exosomes initiate primary osteosarcoma lung metastasis by transferring the miR-194/215 cluster targeting MARCKS, making the miR-194/215 cluster a promising therapeutic target for inhibiting the progression of patients with osteosarcoma lung metastases.

*Corresponding authors.
E-mail addresses: cpu_lykong@126.com (Lingyi Kong), zhangchao@cpu.edu.cn (Chao Zhang).

1. Introduction

Osteosarcoma, a prevalent primary malignant bone tumor, frequently culminates in distant metastasis, particularly to the lungs. Research has revealed that an estimated 15%−20% of patients with osteosarcoma have distant metastases at the time of diagnosis, with pulmonary metastases accounting for more than 85% of these cases[1]. The survival rate of these patients is critically impacted due to the unmanageable nature of lung metastases, despite standard treatment[2]. This phenomenon is further complicated by the high heterogeneity and redundancy of growth signals in osteosarcoma, contributing to the dearth of efficacious molecular therapeutic targets[3]. The intricate pathological and molecular mechanisms driving osteosarcoma lung metastasis remain largely elusive, posing significant challenges to effective treatment[4].

Beyond the inherent attributes of cancer cells, the interplay between the lung microenvironment and cancer cells orchestrates the evolution and development of lung lesions[5]. Tumor cells can induce detrimental alterations in lung remodeling, establishing a malignant cycle conducive to the expansion of disseminated lung tumor cells[6]. Interestingly, the lung microenvironment can reprogram tumor cells, endowing them with characteristics distinct from the primary tumor, thereby propelling secondary metastasis[7]. Advancements in understanding the cascade reaction of cancer lung metastasis have led to paradigm shifts in patient treatment strategies[8]. Evidence shows that CXCL1, secreted by human pulmonary artery endothelial cells, enhances the motility of osteosarcoma cells by upregulating VCAM-1 expression, thereby amplifying osteosarcoma cell homing to the lungs[9]. Furthermore, the lysosomal degradation of the Rab22A-NeoF1 fusion protein, targeted by PINK1, has been shown to impede the migration and invasion of osteosarcoma cells, thereby inhibiting lung metastasis[10]. Nevertheless, therapeutic approaches for osteosarcoma lung metastasis remain limited and predominantly palliative. The role of lung−bone transmission in the prognosis and progression of patients with osteosarcoma lung metastasis is yet to be comprehensively understood.

Exosomes, extracellular vesicles approximately 50−150 nm in diameter secreted by eukaryotic cells, have emerged as potent biomarkers for early diagnosis and prognosis prediction in osteosarcoma[11]. They play critical roles in the orchestration of tumor development, modulating cell growth, metastasis, and angiogenesis through the transmission of bioactive cargoes, encompassing lipids, proteins, and regulatory RNAs[12]. Notably, BMSC-derived exosomal miR-769-5p has been reported to propel osteosarcoma metastasis by targeting DUSP16[13], and the reduction in miR-135a in osteosarcoma has been associated with the inhibition of osteosarcoma progression and lung metastasis[14]. However, the reported effects of individual miRNAs exhibit significant discrepancies[15,16], undermining their efficacy as therapeutic targets. Conversely, miRNA clusters, comprising adjacent miRNA genes sharing the same transcriptional regulation, present a promising avenue for reliable biomarker development[15]. The role of exosomal miRNA clusters in osteosarcoma metastasis and their impact on primary tumor progression, particularly those emanating from lung metastasis sites, remains uncharted territory.

Myristoylated alanine-rich C-kinase substrate (MARCKS), a substrate for protein kinase C, interacts with calcium/calmodulin and crosslinks with F-actin, thereby regulating the interplay between actin and membranes and ensuring the dynamic equilibrium of the actin network[17]. While MARCKS has been implicated in cancer metastasis, its role exhibits heterogeneity across different malignancies, potentially attributable to variations in tumor origin and cell type[18−21]. Furthermore, research has demonstrated that MARCKS can also modulate edematous lung injury by affecting the expression of ENaC through the PI3K/AKT signaling pathway[22]. The role of MARCKS in regulating lung−bone transmission and its subsequent impact on lung metastasis during osteosarcoma progression presents an unresolved area of investigation.

In this study, it was elucidated that exosomes from the pulmonary metastasis site of osteosarcoma can facilitate the translocation of the miR-194/215 cluster to primary osteosarcoma via the "lung−bone" transmission. These occurrences stimulate epithelial−mesenchymal transition (EMT) and vasculogenic mimicry (VM) formation by engaging the MARCKS/PHLPP/p-AKT/Slug signaling pathway, hence facilitating secondary metastasis. Hence, the interception of the miRNA "lung−bone" transmission mediated by osteosarcoma exosomes emerges as a compelling strategy for mitigating osteosarcoma metastasis. To leverage this strategy, in this study, bioengineered exosome mimetics were designed with the aim of "hijacking" this transmission process. These exosome mimetics, fabricated using nucleic acid-depleted exosome membranes from the pulmonary metastasis site of osteosarcoma, can competitively inhibit the functionality of such exosomes from a metastasis site without inducing secondary metastasis. Furthermore, cationic bovine serum albumin (CBSA) was employed as a vehicle for the miR-194/215 cluster antagonist (anta-194/215), enabling it to traverse vesicle membranes due to its positive charge, subsequently forming anta-194/215-loaded exosome mimetics (anta-194/215@Exo). Experimental data illustrate that these bioengineered exosome mimetics (anta-194/215@Exo) efficaciously "block" the "lung−bone" transmission of the miR-194/215 cluster, subsequently inhibiting the advancement of osteosarcoma and notably prolonging the lifespan of tumor-bearing mice. Given the close association of exosome-mediated lung-primary focus axes with the metastasis of various malignancies, including breast cancer[23], melanoma[24], and pancreatic cancer[25], this "hijacking" therapeutic strategy using artificial exosome imitations could extend to multiple types of cancer, thereby offering a promising new approach for anticancer treatment.

2. Materials and methods

2.1. Patient sample procurement

An osteosarcoma tissue microarray (No. L714901) was sourced from Bioaitech Co., Ltd. (Xi'an, China) with written informed consent, and relevant clinical and pathological data were subsequently collected from these tissue samples. The employment of these tissue specimens received authorization from the Ethics Committee of China Pharmaceutical University (Nanjing, China).

2.2. Cell cultivation and procurement of reagents

U-2OS and HOS human osteosarcoma cells were sourced from the Cell Bank of the Chinese Academy of Sciences (Shanghai, China). Human umbilical vein endothelial (HUVEC) cells and 143B osteosarcoma cells were obtained from FuHeng Biology (Shanghai, China). These cells were cultivated in specific media: RPMI-1640 (U-2OS), DMEM (HOS), F12K (HUVEC), and MEM (143B), each supplemented with 10% fetal bovine serum and a 1% penicillin−streptomycin mix (Beyotime Biotechnology). Cells were cultivated in an incubator maintained at 37 °C with 5% CO_2. All cell lines were tested for mycoplasma every other week using the MycoAlert Mycoplasma Detection Kit (Lonza). The chemical reagents Dynasore, 5,6-dichlorobenzimidazole riboside (DRB), and perifosine were procured from CSNpharm (Chicago, IL, USA), with purity levels exceeding 98%.

2.3. Exosome purification

To generate a gradient of iodixanol solutions, 50% (w/v), 40% (w/v), and 10% (w/v) iodixanol solutions were prepared by diluting OptiPrep™ (Stemcell™ Technologies) with 0.85% sodium chloride and 10 mmol/L Tris−HCl, pH 7.4. The exosomes were resuspended in 3.8 mL of 50% iodixanol solution, overlaid with 3 mL of 40% solution, and then 2.5 mL of 10% solution in a centrifuge tube. The gradient was then centrifuged at $200,000 \times g$ for 2 h at 4 °C. Ten gradient fractions were diluted in PBS and centrifuged at $110,000 \times g$ for 70 min at 4 °C. They were then resuspended in a lysis buffer (Yeasen Biotechnology). The density was determined gravimetrically (g/mL).

2.4. Transmission electron microscope (TEM) analyses

A volume of 10 μL of the purified exosomes was applied to a copper mesh grid, and allowed to settle for 3−5 min, after which the adjacent liquid was absorbed with filter paper. Subsequently, ten microliters of phosphotungstic acid were added, allowed to stand for another 5 min, and air-dried before observation under a TEM (Hitachi).

2.5. miRNA fluorescence in situ hybridization

Standard fluorescence in situ hybridization was utilized for the detection of miR-194-5p and miR-215-5p expression in human osteosarcoma tissue[26]. Biotinylated 5′-end oligonucleotide probes specific for miR-194-5p and miR-215-5p (5′-TCCA-CATGGAGTTGCTGTTACA-3′ and 5′-GTCTGTCAATTCA-TAGGTCAT-3′) were used. Post-slide washing with sodium citrate solution and PBST (PBS with 0.1% Tween-20), positive hybridization signals were visualized using fluorescein isothiocyanate-labeled avidin. Images were acquired using the ImageXpress® Micro Confocal System (Molecular Devices) and analyzed with MetaXpress software (Molecular Devices).

2.6. Exosome membrane preparation and characterization

As outlined in the referenced protocol[27], purified exosomes were resuspended in an ice-cold Tris (0.01 mol/L)-Mg (0.001 mol/L $MgCl_2$) buffer, exposed to five or more freeze−thaw cycles, then rinsed with a cold Tris-Mg buffer containing 0.25 mol/L sucrose, and centrifuged at $3000 \times g$ for 30 min at 4 °C. Parameters including the particle size, polydispersity index (PDI), and zeta potential of exosome membranes were assessed using a Malvern Nano ZS90 Particle Size Analyzer (Malvern).

2.7. Formation and evaluation of anta-miRNA@Exo nanoparticles

CBSA-anta-miRNA nanoparticles were encapsulated within exosome membranes through an incubation and extrusion technique, yielding anta-miRNA@Exo. The CBSA-anta-miRNA nanoparticles and exosome membranes were initially co-incubated at 4 °C for 30 min, then agitated and incubated at 37 °C for an hour. The mixture was subsequently co-extruded through a 200-nm polycarbonate membrane 20 times to generate the anta-miRNA@Exo nanoparticles. The resultant nanoparticles were analyzed in terms of particle size, PDI, and zeta potential using a Malvern Nano ZS90 Particle Size Analyzer.

2.8. Animal studies

All animal experiments were conducted following the protocol approved by the Institutional Animal Care and Use Committee at China Pharmaceutical University (Permit Number: 2020-06-006). To investigate the effect of HOS-Exo or HOS-LuT3-Exo on in vivo osteosarcoma lung metastasis, $HOS^{GFP-Luc}$ cells (5×10^5) and HOS-Exo or HOS-LuT3-Exo (1.25×10^{10} particles) were co-cultured in vitro for 24 h. Subsequently, the cells were co-injected into mice via the tail vein, supplemented with an additional 1.25×10^{10} exosomes. Specifically, male NCG-HLA-A2.1 mice (GemPharmatech), aged six to eight weeks, were randomly assigned into three groups (six mice per group). The IVIS Lumina Series III bioluminescence imaging system (PerkinElmer) was utilized for in vivo detection of HOS cell metastasis to the lung after two weeks, with analysis carried out using Living Image Software (PerkinElmer). The degree of lung metastasis was assessed via HE staining of paraffin-embedded lung slices.

To investigate the impact of exosomes derived from osteosarcoma under varying treatments on tumor metastasis and VM formation, an orthotopic injection of HOS cells into the tibia of 6−8-week-old male NCG-HLA-A2.1 mice was executed. Exosomes (1.25×10^{10} particles in 200 μL) were delivered intravenously every three days, totaling five injections, initiated three days post-injection. On the 28th day, mice were euthanized and tumors as well as lung tissues were collected for subsequent analysis.

2.9. Statistical analysis

All experiments were independently conducted at least three times, and the data are presented as mean ± standard deviation. All statistical evaluations were executed using GraphPad Prism 8.0. A Student's t-test was employed for comparisons between two groups, and one-way ANOVA was used for comparisons among multiple groups to discern differences. (*$P < 0.05$, **$P < 0.01$, ***$P < 0.001$; #$P < 0.05$, ##$P < 0.01$, ###$P < 0.001$; ns, not significant).

3. Results

3.1. The role of osteosarcoma lung metastasis-derived exosomes in facilitating secondary pulmonary metastasis via lung−bone transmission

Considering the critical function of exosomes in interorgan signaling, the influence of exosomes derived from osteosarcoma

lung metastasis sites on primary osteosarcoma was investigated, particularly in the context of disease progression. Starting from parental osteosarcoma (HOS) cells, a reliable animal model of osteosarcoma lung metastasis was constructed, and a subpopulation of osteosarcoma cells from lung metastasis loci, termed HOS-LuT3 cells, was isolated (Supporting Information Fig. S1A). Both HOS$^{CD63-pEGFP}$ cells and their lung metastasis progeny, HOS-LuT3$^{CD63-pEGFP}$ cells, secreted EGFP$^+$ exosomes. Ultrahigh-speed centrifugation paired with iodixanol/Optiprep gradient density centrifugation was used for exosome separation from HOS and HOS-LuT3 cell supernatants. The presence of exosomal markers (CD9, CD63, TSG101, ALIX, and MHC-I) in fractions 2−3, with a higher marker concentration and a density of 1.10 g/mL in fraction 3, was confirmed (Fig. S1B). Western blot, nanoparticle tracking analysis, and TEM validated the biological markers, size, and distinctive structure of exosomes secreted from HOS and lung metastasis-associated osteosarcoma (HOS-LuT3) cells (Fig. S1C−S1E). The uptake of exosomes by osteosarcoma cells was studied by treating HOS cells with PKH67-labeled HOS-LuT3 exosomes (HOS-LuT3-Exo) and using HOS exosomes (HOS-Exo) as a control. Over 90% of HOS cells exhibited PKH67 fluorescence after 24 h of incubation with exosomes, with no significant difference between the uptake of HOS-Exo and HOS-LuT3-Exo (Fig. S1F).

A central role for the lung−primary lesion axis in the progression of primary diseases was posited. To examine the uptake of exosomes from lung metastasis sites by primary osteosarcoma, HOS cells were introduced into the tibia, followed by injection into the lung with PBS, HOS$^{CD63-pEGFP}$ shNC cells, HOS-LuT3$^{CD63-pEGFP}$ shNC cells, or Rab27a-silenced (for exosome secretion inhibition) HOS-LuT3$^{CD63-pEGFP}$ cells, establishing a lung lesion osteosarcoma animal model (Supporting Information Fig. S2A). Clear EGFP signaling was observed in situ in osteosarcoma cells in the HOS-LuT3$^{CD63-pEGFP}$ shNC group mice, and no substantial EGFP signal was detected in other groups, signifying that CD63-pEGFP exosomes secreted by HOS-LuT3 cells were internalized by primary osteosarcoma cells (Fig. 1A). To avoid any potential ambiguity caused by the EGFP signal of autologous tumor cells, PKH26-labeled exosomes (HOS-LuT3-Exo) were administered intravenously into mice with in situ osteosarcoma (Fig. S2B). The concentrated bioluminescence imaging (BLI) signal within bone tumors indicates that exosomes can be taken up by osteosarcoma cells in situ through blood circulation (Fig. 1B).

Numerous studies suggest that tumor-derived exosomes modulate EMT processes, promoting cancer progression[28]. VM, which provides blood supply for tumors, correlates with poor prognosis in malignancies such as osteosarcoma[29,30]. EMT regulatory factors are highly expressed in VM-forming tumor cells, highlighting the crucial role of EMT in VM development in osteosarcoma[30,31]. The influence of osteosarcoma exosomes from lung metastasis sites on osteosarcoma EMT and VM formation was examined by pretreating HOS cells with HOS-LuT3-Exo for 24 h, with HOS-Exo and PBS serving as controls (Fig. 1C). Colony formation assays showed that neither HOS-Exo nor HOS-LuT3-Exo impacted osteosarcoma cell proliferation (Supporting Information Fig. S3A). However, the tubule formation capacity of HOS cells was significantly enhanced by HOS-LuT3-Exo (Fig. 1D and E). To simulate the barrier-crossing steps in tumor metastasis directly, a monolayer model of HUVECs grown on a filter membrane was used to assess the transendothelial invasion capability of cancer cells (Fig. S3B)[32]. After HOS-LuT3-

Exo treatment, the number of GFP-labeled HOS cells penetrating the HUVEC monolayer increased significantly compared to that in the HOS-Exo group (Fig. 1F and G). Western blot and immunofluorescence analyses showed higher expression of EMT markers (N-cadherin and Vimentin) and a VM marker (VE-Cadherin) in osteosarcoma cells treated with HOS-LuT3-Exo than in control cells treated with HOS-Exo or PBS (Fig. 1H and Fig. S3C). Additionally, HOS-LuT3-Exo-treated HOS cells were injected intravenously into mice (Fig. S3D). In mouse BLI and lung tissue sections, there was a significant increase in lung metastasis foci following HOS-LuT3-Exo treatment compared with that after treatment with HOS-Exo or PBS, suggesting a role for osteosarcoma exosomes from lung metastasis sites in promoting the metastasis of in situ osteosarcoma (Fig. S3E and S3F). The role of these osteosarcoma exosomes in promoting osteosarcoma metastasis along the lung−bone transmission was further demonstrated by injecting in situ osteosarcoma-bearing mice every three days with equal amounts of HOS-Exo or HOS-LuT3-Exo (Fig. 1I). Tumor weight and Ki67 staining indicated a minor but nonsignificant increase in tumor burden in the HOS-LuT3-Exo group, implying that HOS-LuT3-Exo does not induce in situ osteosarcoma proliferation (Fig. 1J and Supporting Information Fig. S4). VM is typically identified by CD31-negative and PAS-positive cancer cell arrangements and the presence of red blood cells in the lumen[33,34]. Interestingly, CD31/PAS dual staining showed that the formation of VM channels in in situ osteosarcoma was significantly higher in mice treated with HOS-LuT3-Exo than in mice treated with HOS-Exo or PBS (Fig. 1J). Western blot analysis showed significant upregulation in the expression of N-cadherin, Vimentin, and VE-Cadherin proteins in the in situ osteosarcoma of the HOS-LuT3-Exo group compared with the in situ osteosarcoma of the control group (Fig. 1K). Moreover, Bouin's staining and H&E staining of lung tissue showed a significant increase in the number and area of in situ osteosarcoma lung metastasis foci following stimulation with HOS-LuT3-Exo (Fig. 1L). Thus, it can be concluded that exosomes derived from lung metastasis sites of osteosarcoma can induce VM formation driven by EMT in situ in osteosarcoma, thereby endowing them with unique characteristics distinct from primary cancer and promoting secondary lung metastasis of osteosarcoma.

3.2. Elevated expression of the miR-194/215 cluster in pulmonary metastatic osteosarcoma cells and associated exosomes

Exosomes rich in miRNAs play vital roles in cell-to-cell communication[35]. miRNA clusters, chromosomally organized gene collections, offer enhanced regulatory markers over individual miRNAs[15]. Notably, U-2OS cells are low-metastatic osteosarcoma lines[36], and 143B cells are high-pulmonary metastatic lines[37]. Through a comparison of the VM formation capability driven by EMT across four osteosarcoma cells (Supporting Information Fig. S5A and S5B), U-2OS cells and associated exosomes were established as negative controls, whereas 143B cells and their corresponding exosomes were designated as positive controls. A miRNA microarray analysis was utilized to identify disparate miRNA expression patterns in U-2OS-Exo, HOS-Exo, and HOS-LuT3-Exo. Notably, compared with HOS-Exo and U-2OS-Exo, for HOS-LuT3-Exo, there were 73 and 90 upregulated miRNAs, respectively (Supporting Information Fig. S6). Of these significantly amplified miRNAs,
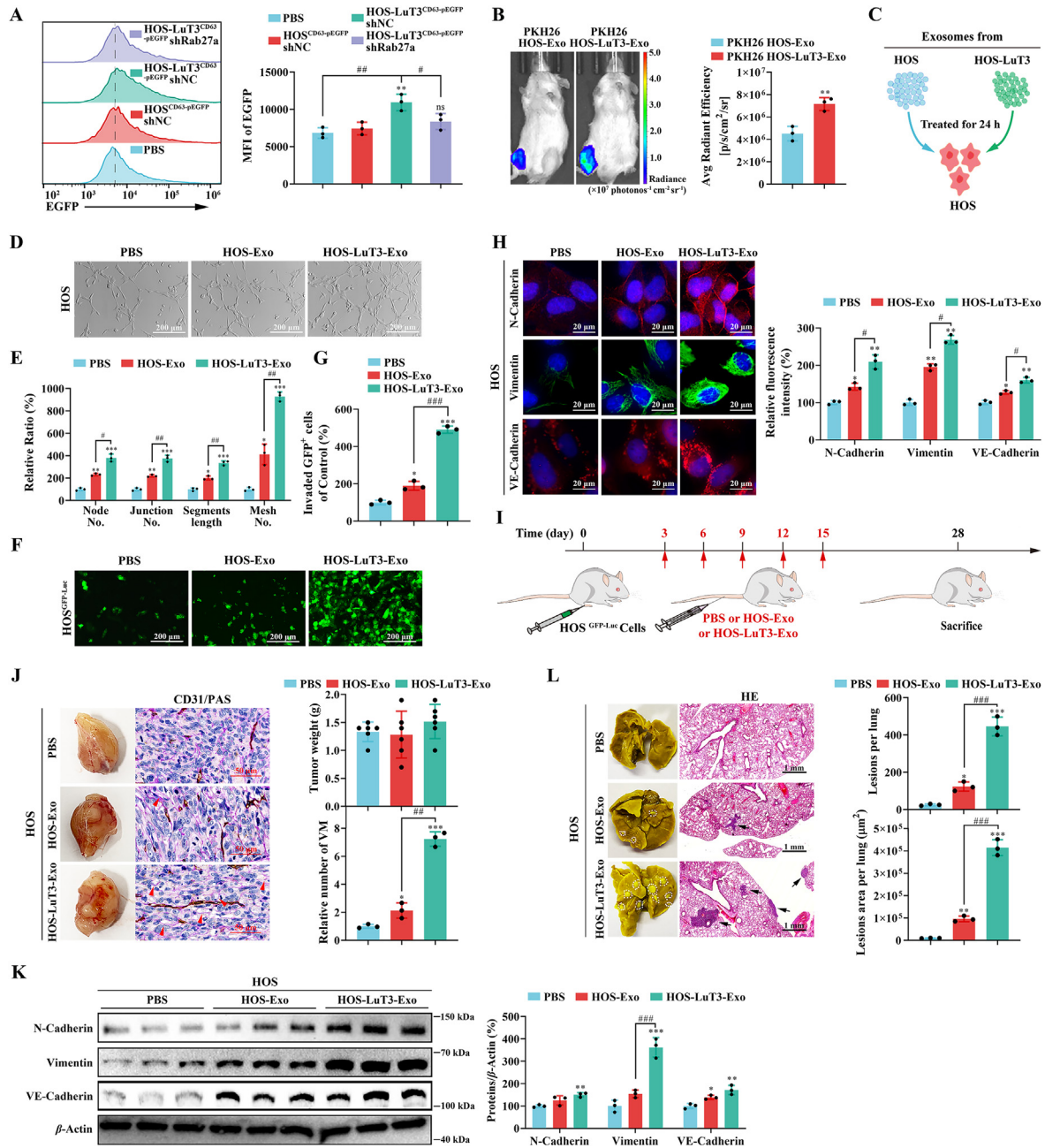
Figure 1 Pulmonary metastatic osteosarcoma exosomes accumulate in the primary tumor site and exacerbate osteosarcoma progression. (A) Mouse bone implantation with HOS cells followed by pulmonary introduction of designated cells after 14 days led to pulmonary lesion formation ($n = 6$). Flow cytometric assessment of EGFP signals in osteosarcoma orthotopic transplant tumor tissue ($n = 3$). (B) Intravenous introduction of PKH26-labelled exosomes into mice bearing orthotopically implanted HOS cells ($n = 3$). Representative bioluminescence images and quantification of the mouse BLI signal ($n = 3$). (C) Illustration of HOS and HOS-LuT3 cell-derived exosome treatment regimen on HOS cells over 24 h. (D−H) HOS cells subjected to treatment with PBS, HOS-Exo, or HOS-LuT3-Exo ($n = 3$). (D) Representative images of tube formation (Scale bar = 200 nm). (E) Quantitative assessment of tube formation. (F) Representative images of transendothelial invasion (Scale bar = 200 nm). (G) Quantitative evaluation of GFP$^+$ HOS cells penetrating through the HUVEC monolayer. (H) Immunofluorescence evaluation of Vimentin, N-Cadherin, and VE-Cadherin expression (DAPI in blue; Vimentin in green; N-Cadherin and VE-Cadherin in red. Scale bar = 20 μm). (I−L) Tibial implantation of HOS cells in NCG-HLA-A2.1 male mice. Following a 3-day interval, intravenous injections of PBS, HOS-Exo, or HOS-LuT3-Exo were administered every 3 days ($n = 6$). (I) Illustration of the orthotopic osteosarcoma animal model with exosome treatment. (J) Representative images of mouse tumors and CD31/PAS staining in tumor tissue (Scale bar = 50 μm), alongside tumor weight quantification ($n = 6$) and relative quantification of VM ($n = 3$). (K) Western blot assessment of N-Cadherin, Vimentin, and VE-Cadherin protein expression levels in tumor tissues ($n = 3$). (L) Representative images of mouse lungs and HE staining in lung tissue (Scale bar = 1 mm), in conjunction with quantification of lung metastatic foci ($n = 3$). The data are presented as the mean ± SD. *$P < 0.05$, **$P < 0.01$, ***$P < 0.001$; ns, not significant vs. the PBS group. #$P < 0.05$, ##$P < 0.01$, ###$P < 0.001$.
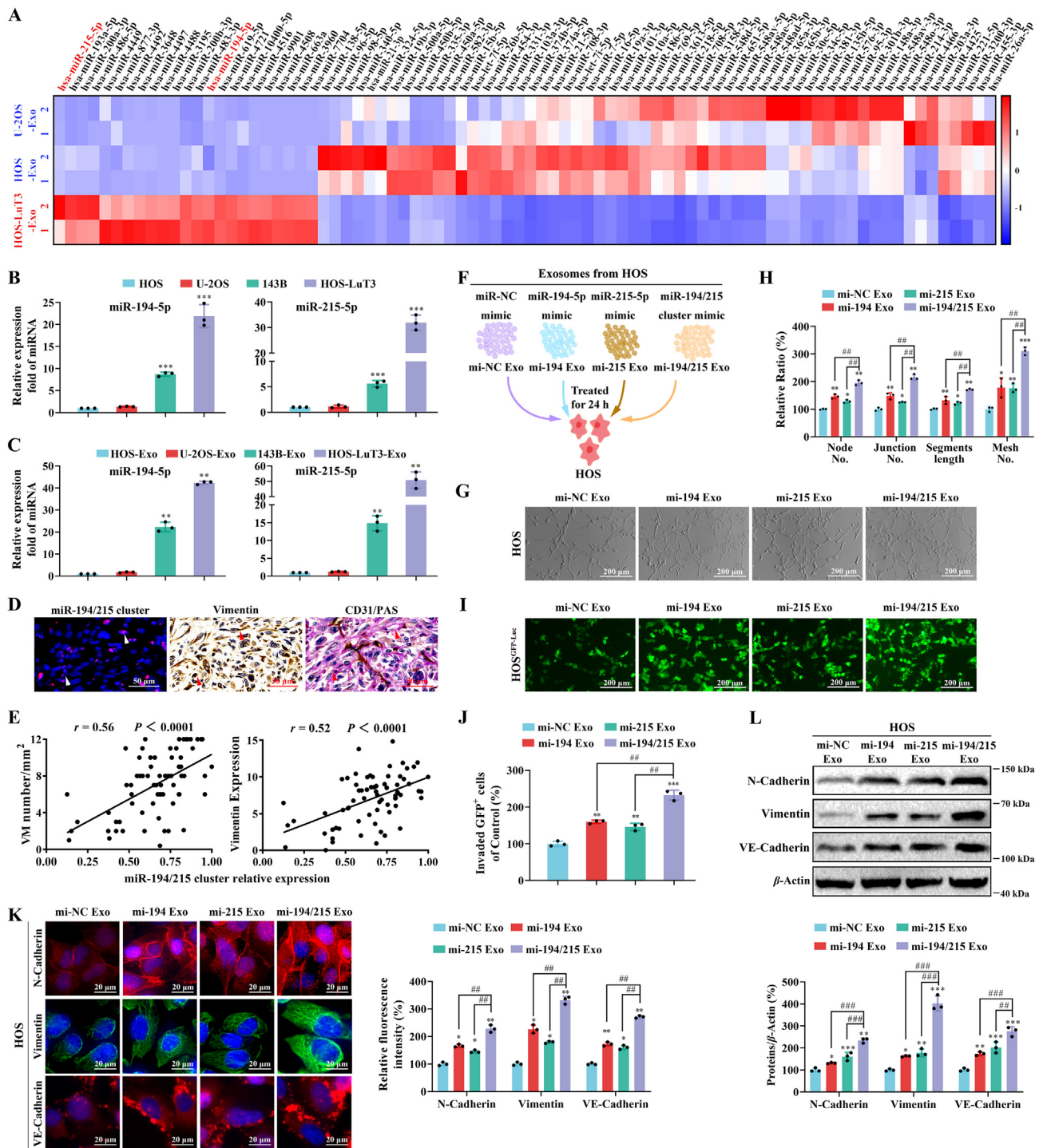
Figure 2 miR-194/215 cluster exhibits upregulation in lung metastatic osteosarcoma cells and exosomes. (A) Heatmap presentation of the microarray analysis of exosomal miRNAs originating from HOS, U-2OS, and HOS-LuT3 cells ($n = 2$). (B) RT-qPCR employed for the assessment of miR-194-5p and miR-215-5p expression in HOS, U-2OS, 143B, and HOS-LuT3 cells ($n = 3$). (C) RT-qPCR utilized for evaluating miR-194-5p and miR-215-5p expression in HOS, U-2OS, 143B, and HOS-LuT3 exosomes ($n = 3$). (D, E) Examination of tumor samples from 70 cases of osteosarcoma patients. (D) Representative images of miR-194/215 cluster, Vimentin, and CD31/PAS at identical locations in osteosarcoma tissue samples (Scale bar = 50 μm). (E) Correlation analysis between miR-194/215 cluster levels and VM density ($r = 0.56$, $P < 0.0001$), and Vimentin protein levels ($r = 0.52$, $P < 0.0001$) in osteosarcoma patients. (F) Schematic representation of the effect of exosomes derived from HOS cells transfected with miR-NC, miR-194-5p, miR-215-5p, or miR-194/215 cluster mimic on HOS cells over 24 h. (G–L) HOS cells subjected to treatment with mi-NC Exo, mi-194 Exo, mi-215 Exo, or mi-194/215 Exo ($n = 3$). (G) Representative images and (H) quantification of tube formation (Scale bar = 200 μm). (I) Representative images of transendothelial invasion (Scale bar = 200 μm). (J) Quantitative evaluation of GFP$^+$ HOS cells penetrating through the HUVEC monolayer. (K) Immunofluorescence examination of Vimentin, N-Cadherin, and VE-Cadherin expression (DAPI in blue; Vimentin in green; N-Cadherin and VE-Cadherin in red. Scale bar = 20 μm). (L) Western blot analysis of Vimentin, N-Cadherin, and VE-Cadherin expression. The data are presented as the mean ± SD. $*P < 0.05$, $**P < 0.01$, $***P < 0.001$ *vs.* the HOS, HOS-Exo or mi-NC Exo group. $^{##}P < 0.01$, $^{###}P < 0.001$.

miR-194-5p and miR-215-5p alone were derived from the same miRNA cluster, and miR-7704 and miR-3960 were the most abundant (Fig. 2A). Real-time quantitative PCR (RT-qPCR) assays verified the overexpression of miR-194-5p and miR-215-5p in both HOS-LuT3 cells and exosomes (Fig. 2B and C), suggesting a plausible role of the miR-194/215 cluster in VM formation propelled by EMT of osteosarcoma *in situ* and stimulated by exosomes from pulmonary metastatic osteosarcoma.

Upregulation of miR-194-5p, miR-215-5p, miR-7704 and miR-3960 was implemented using miR-194-5p, miR-215-5p, miR-7704 and miR-3960 mimics (mi-194, mi-215, mi-7704 and mi-3960) (Supporting Information Fig. S7A and S7B). The ensuing tube formation and transendothelial invasion experiments revealed an amplified capacity for tube-like structure creation and endothelium penetration in osteosarcoma cells expressing elevated levels of the miR-194/215 cluster but not miR-7704 and miR-3960 (Fig. S7C−S7H). Immunofluorescence analysis further indicated that the overexpression of the miR-194/215 cluster promoted the expression of EMT and VM markers, characterized by increases in N-cadherin, Vimentin, and VE-Cadherin levels (Fig. S7I). The clinical relevance of the miR-194/215 cluster in VM formation propelled by osteosarcoma EMT was investigated using paraffin-embedded, formalin-fixed tumor samples from 70 osteosarcoma patients. A correlation analysis revealed significant associations between Vimentin protein levels ($P = 0.023$), VM density ($P = 0.038$), and miR-194/215 cluster levels ($P = 0.030$) with TNM staging, but not with age (Table 1). Tissues exhibiting high levels of the miR-194/215 cluster had high Vimentin protein levels and a high VM density (Fig. 2D). Out of the 70 osteosarcoma samples, 24 out of 35 cases (69%) in the miR-194/215 cluster-high group had a high VM density, and 25 cases (71%) had high Vimentin protein levels. Conversely, in the miR-194/215 cluster-low group, high VM density was observed in 16 out of 35 cases (46%), and elevated Vimentin levels were observed in 15 cases (43%). Statistical analyses corroborated a positive correlation between miR-194/215 cluster levels and VM density ($r = 0.56$, $P < 0.0001$) and Vimentin protein level ($r = 0.52$, $P < 0.0001$) (Fig. 2E).

To ascertain the effect of osteosarcoma exosomes bearing the miR-194/215 cluster on EMT and VM formation in osteosarcoma cells, exosomes were isolated from the conditioned medium of HOS cells transfected with mi-194, mi-215, mi-194/215, or mi-NC, and miR-194-5p and miR-215-5p were quantified in these exosomes using RT-qPCR. The results suggest that cells transfer the miR-194/215 cluster into exosomes during their formation (Supporting Information Fig. S8A). *In vivo* and *in vitro* analyses were performed using exosomes released by HOS cells transfected with mi-NC, mi-194, mi-215, or mi-194/215, and then applied to HOS cells (Fig. 2F). The findings revealed that mi-194/215 Exo considerably enhanced the tube formation and transendothelial invasion capacity of HOS cells (Fig. 2G−J) and induced the protein expression of N-Cadherin, Vimentin, and VE-Cadherin (Fig. 2K and L). In a subsequent study, HOS cells treated with mi-NC Exo, mi-194 Exo, mi-215 Exo, and mi-194/215 Exo were injected intravenously into mice (Fig. S8B). The resulting enriched BLI signal in the lungs and H&E staining results suggested that mi-194/215 Exo significantly fostered an increase in pulmonary metastatic foci (Fig. S8C and S8D), thereby indicating that the miR-194/215 cluster in exosomes of pulmonary metastatic osteosarcoma induces *in situ* osteosarcoma metastasis.

3.3. The miR-194/215 cluster facilitates metastasis via pulmonary metastatic lesion osteosarcoma exosomes through lung−bone transmission

The possibility of miR-194/215 clusters housed within pulmonary metastatic lesion osteosarcoma exosomes being transferred to osteosarcoma cells was explored. Transfection of HOS-LuT3 cells with Cy5 and FAM-tagged mi-194 and mi-215, respectively, was followed by culturing HOS cells in the presence of exosomes secreted from these transfected cells. Fluorescence imaging confirmed significant cytoplasmic colocalization of Cy5 and FAM signals within HOS cells (Fig. 3A). Furthermore, RT-qPCR analysis showed higher miR-194-5p and miR-215-5p expression in HOS cells treated with HOS-LuT3-Exo than in those treated with HOS-Exo, regardless of transcription inhibitor (DRB) usage (Supporting Information Fig. S9A). In contrast, the endocytosis inhibitor (Dynasore) blocked HOS-LuT3-Exo-induced miR-194-5p and miR-215-5p expression (Fig. S9A); this implies that miR-194/215 cluster transportation is exosome dependent and not contingent on endogenous miRNA transcription, enabling pulmonary metastatic lesion osteosarcoma exosomes to deliver the miR-194/215 cluster to *in situ* osteosarcoma cells.

To discern the influence of the miR-194/215 cluster in pulmonary metastatic lesion osteosarcoma exosomes on primary osteosarcoma cells, exosomes from HOS-LuT3 cells transfected

Table 1 Correlation between VM density, Vimentin, miR-194/215 cluster, and clinicopathologic characteristics of patients with osteosarcoma.

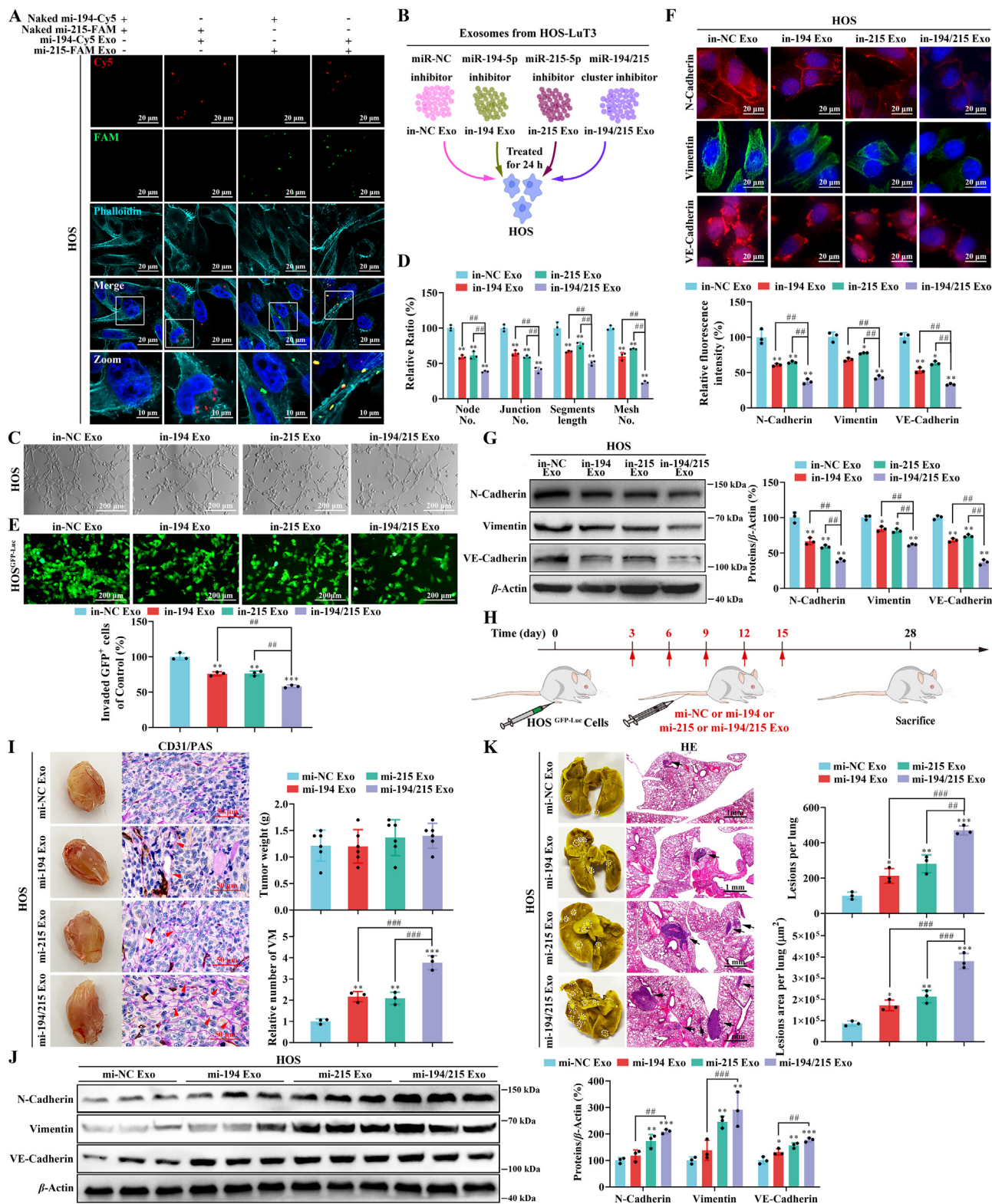| clinicopathologic characteristics		Age (years)		TNM Stage	
		≥30	≤30	IA/IIA	IIB/IVB
n (%)		30 (43%)	40 (57%)	33 (47%)	37 (53%)
VM density	Low (n)	14	16	14	16
	High (n)	16	24	19	21
	P	0.40		0.038	
Vimentin	Low (n)	12	18	15	15
	High (n)	18	22	18	22
	P	0.48		0.023	
miR-194/215 cluster	Low (n)	17	18	19	16
	High (n)	13	22	14	21
	P	0.49		0.030	

*Statistically significant $P < 0.05$.

Figure 3 miR-194/215 cluster facilitates pro-metastatic effects of exosomes in lung metastatic osteosarcoma cells. (A) Fluorescence images of HOS cells incubated with exosomes derived from HOS-LuT3 cells transfected with Cy5-labeled miR-194-5p or FAM-labeled miR-215-5p, or with naked Cy5-labeled miR-194-5p or naked FAM-labeled miR-215-5p (Scale bar = 20 μm). (B) Diagram showcasing the influence of exosomes derived from HOS-LuT3 cells transfected with miR-NC, miR-194-5p, miR-215-5p, or miR-194/215 cluster inhibitor on HOS cells over 24 h. (C−G) HOS cells are subject to treatment with in-NC Exo, in-194 Exo, in-215 Exo, or in-194/215 Exo (n = 3). (C) Representative images and (D) quantification of tube formation (Scale bar = 200 μm). (E) Representative images and quantification of transendothelial invasion (Scale bar = 200 μm). (F) Immunofluorescence investigation of the expression of Vimentin, N-Cadherin, and VE-Cadherin (DAPI in blue; Vimentin in

with miR-NC inhibitor (in-NC), miR-194-5p inhibitor (in-194), miR-215-5p inhibitor (in-215), and miR-194/215 cluster inhibitor (in-194/215) were isolated and subsequently applied to HOS cells (Fig. 3B). Transfection efficiencies were confirmed (Fig. S9B). Compared to in-NC Exo, in-194 Exo, and in-215 Exo, in-194/215 Exo treatment notably hindered tube formation and transendothelial invasion in HOS cells (Fig. 3C—E). Through immunofluorescence and western blotting, it was found that in-194/215 Exo suppressed the protein expression of N-Cadherin, Vimentin, and VE-Cadherin in HOS cells (Fig. 3F and G). These data imply that pulmonary metastatic lesion osteosarcoma exosomes bearing the miR-194/215 cluster can drive the metastasis of primary osteosarcoma cells *via* lung—bone transmission.

Moreover, an *in situ* osteosarcoma model was established by inoculating NCG mice with HOS cells. Exosomes from HOS cells, transfected with mi-NC, mi-194, mi-215, or mi-194/215, were periodically administered through tail vein injection (Fig. 3H). Tumor weight measurements, Ki67 staining, and CD31/PAS dual staining of tumor tissues showed that mi-194/215 Exo considerably boosted the development of VM in primary osteosarcoma; however, the effect on proliferation was minimal (Fig. 3I and Supporting Information Fig. S10). Western blot results indicated that mi-194/215 Exo induced the expression of EMT and VM markers in primary osteosarcoma cells (Fig. 3J). Furthermore, Bouin's and H&E's staining of lung tissue indicated a significant increase in the quantity and enlargement of the area of primary osteosarcoma lung metastatic lesions after enhancement of the miR-194/215 cluster in HOS-Exo (Fig. 3K).

3.4. MARCKS emerges as a direct target of the miR-194/215 cluster within pulmonary metastatic osteosarcoma exosomes

Bioinformatics tools, including miRTarBase, miRWalk, TargetScan, and miRDB, were utilized to predict the possible target genes of the miR-194/215 cluster, yielding 44 genes meeting the selection criteria (Fig. 4A). Subsequent transfection of mi-194 and mi-215 into HOS cells facilitated further investigation of the target genes of the miR-194/215 cluster *via* evaluation of the expression of the 44 predicted targets. Remarkably, although *TAOK1* and *TRIM44* could be downregulated by miR-194-5p and miR-215-5p, *MARCKS* was the sole gene that was significantly negatively regulated by both miR-194-5p and miR-215-5p (Fig. 4B). Following sequence alignment of miR-194-5p and miR-215-5p with the full-length MARCKS sequence, the coding sequence of MARCKS was pinpointed as a potential target of the miR-194/215 cluster. To validate this, the binding sites of wild-type and mutant miR-194-5p or miR-215-5p were cloned and inserted into a dual-luciferase vector. HOS cells cotransfected with mi-194 or mi-215 and the wild-type binding site vector displayed a noticeable reduction in luciferase activity (Fig. 4C). This inhibitory effect was absent in HOS cells that were transfected with the mutant binding site vector (Fig. 4C), supporting the conclusion that MARCKS is indeed directly targeted by the

miR-194/215 cluster. The clinical significance of *MARCKS*, *TAOK1*, and *TRIM44* in osteosarcoma was determined using the R2: Genomic Analysis and Visualization Platform (http://r2.amc.nl). This analysis revealed that osteosarcoma patients with lower *MARCKS* expression levels had shorter survival durations, whereas *TAOK1* and *TRIM44* levels did not exhibit a significant correlation with patient survival time (Fig. 4D and Supporting Information Fig. S11). Furthermore, there were negative correlations between MARCKS levels and VM density ($r = -0.43$, $P = 0.0002$) and Vimentin levels ($r = -0.46$, $P < 0.0001$), as established using 70 osteosarcoma patient samples (Fig. 4E and F). The observed underexpression of MARCKS in osteosarcoma cells suggests a potential role in inducing metastasis. To test this hypothesis, we employed small interfering RNA (siRNA) to silence *MARCKS*, *TAOK1*, and *TRIM44* in HOS cells. The efficiency of the knockdown was validated through RT-qPCR and Western blot analysis (Supporting Information Fig. S12A—S12C). Crucially, HOS cells with targeted *MARCKS* silencing, as opposed to *TAOK1* or *TRIM44*, demonstrated a marked increase in tube formation and transendothelial invasion capabilities compared to the control group (siNC) (Fig. 4G and H, Fig. S12D and S12E). Additionally, these cells exhibited elevated expression levels of the mesenchymal markers N-Cadherin, Vimentin, and VE-Cadherin (Fig. 4I and J).

Investigation into the correlation between MARCKS and the miR-194/215 cluster contained within pulmonary metastatic lesion osteosarcoma exosomes commenced with the generation of HOS cells overexpressing MARCKS (Supporting Information Fig. S13A). Remarkably, in HOS cells overexpressing MARCKS, there was a decrease in tube formation and transendothelial invasion induced by exosomes containing the miR-194/215 cluster (Fig. 5A—C). Immunofluorescence experiments revealed that MARCKS overexpression inhibited the protein expression of EMT and VM formation markers induced by mi-194/215 Exo (Fig. 5D). Furthermore, Western blot analysis both *in vivo* and *in vitro* indicated that the protein expression of MARCKS was suppressed by pulmonary metastatic lesion osteosarcoma exosomes (HOS-LuT3-Exo) (Fig. 5E and F). Additionally, exosomes with the miR-194/215 cluster reduced MARCKS protein expression in HOS cells (Fig. 5G and H), and interference with the miR-194/215 cluster in exosomes increased MARCKS protein expression in HOS cells (Fig. S13B). Thus, during osteosarcoma progression, the miR-194/215 cluster held within pulmonary metastatic lesion osteosarcoma exosomes propels secondary lung metastasis of osteosarcoma *via* MARCKS regulation during lung—bone transmission.

3.5. The exosomal miR-194/215 cluster/MARCKS axis initiates metastatic processes via the PHLPP/p-AKT/Slug signaling pathway

Insights into the molecular underpinnings by which MARCKS curbs osteosarcoma metastasis were garnered through Western blot analyses probing the influence of MARCKS on EMT

---

green; N-Cadherin and VE-Cadherin in red. Scale bar $= 20$ μm). (G) Western blot analysis for the expression of Vimentin, N-Cadherin, and VE-Cadherin. (H−K) Implantation of HOS cells in NCG-HLA-A2.1 male mice tibia. Following 3 days, mice were intravenously injected with mi−NC Exo, mi-194 Exo, mi-215 Exo, or mi-194/215 Exo every 3 days ($n = 6$). (H) Schematic depiction of the orthotopic osteosarcoma animal model with exosome treatment. (I) Representative images of mouse tumors and CD31/PAS staining in tumor tissue (Scale bar $= 50$ μm), supplemented with tumor weight quantification ($n = 6$) and relative quantification of VM ($n = 3$). (J) Western blot analysis of N-Cadherin, Vimentin, and VE-Cadherin protein expression levels in tumor tissues ($n = 3$). (K) Representative images of mouse lungs and HE staining in lung tissue (Scale bar $= 1$ mm), accompanied by quantification of lung metastatic foci ($n = 3$). The data are presented as the mean $\pm$ SD. *$P < 0.05$, **$P < 0.01$, ***$P < 0.001$ *vs.* the mi-NC Exo or in-NC Exo group. ##$P < 0.01$, ###$P < 0.001$.
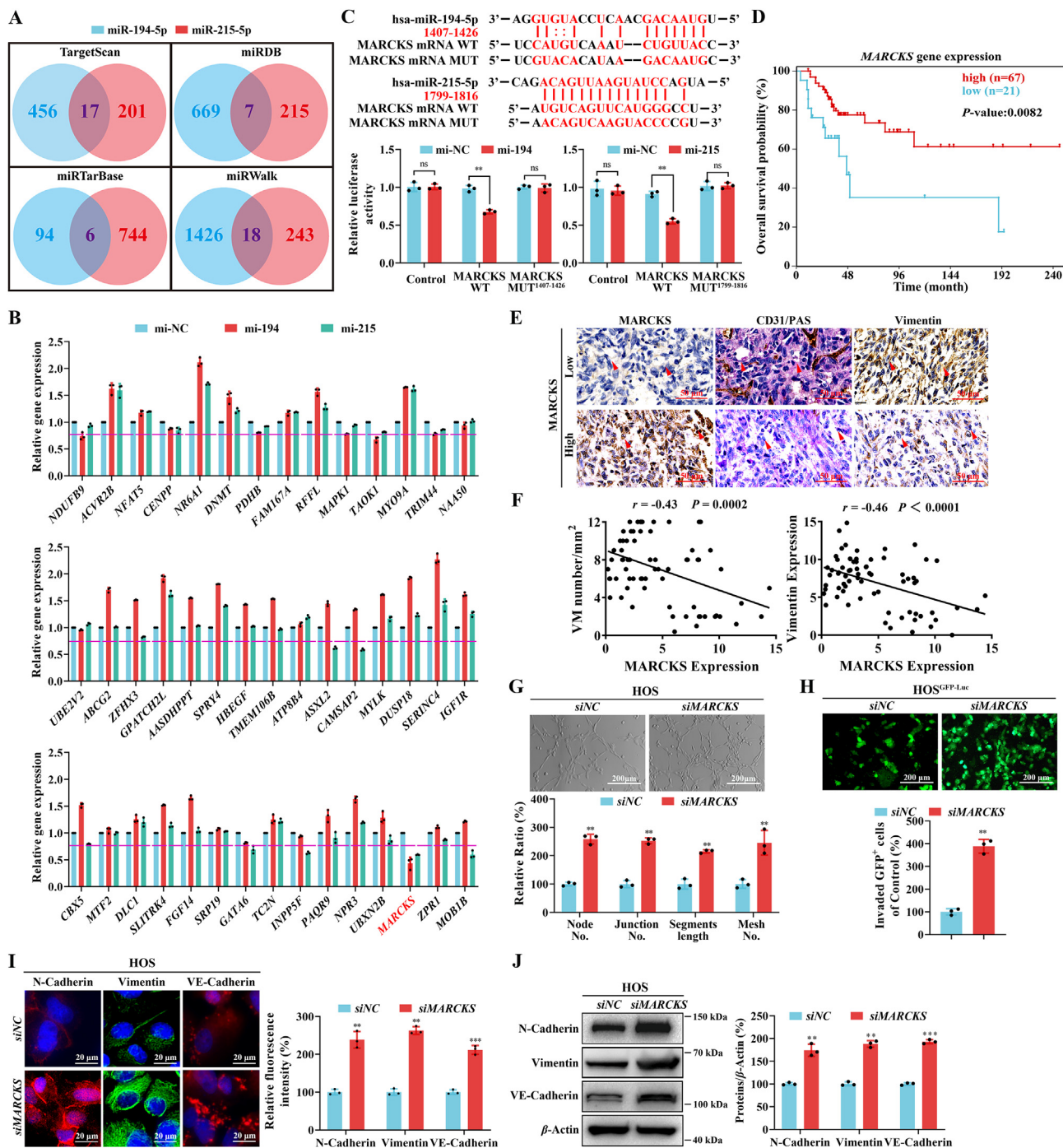
Figure 4 MARCKS represents a target gene of the miR-194/215 cluster housed within exosomes of lung metastatic osteosarcoma cells. (A) Four computational target prediction techniques (TargetScan 7.2, miRDB, miRTarBase, and miRWalk) were deployed to anticipate common target genes for miR-1945p and miR-2155p. (B) RT-qPCR analysis of 44 mRNA expressions in HOS cells transfected with miR-NC, miR-1945p, or miR-2155p mimic (n = 3). (C) Illustration of wild-type (WT) and mutant (MUT) miR-1945p or miR-2155p binding sites within the 3′ UTR of MARCKS, accompanied by corresponding luciferase assay. The relative luciferase activity was gauged in HOS cells post co-transfection with negative control (NC), miR-1945p or miR-2155p mimics, and luciferase reporter plasmids (encasing either MARCKS 3′ UTR WT or MARCKS 3′ UTR MUT) (n = 3). (D) Kaplan−Meier curve indicating overall survival for *MARCKS* expression in osteosarcoma patients (GSE42352, n = 88). (E, F) Tumor samples from 70 osteosarcoma cases. (E) Representative imaging of MARCKS, CD31/PAS, and Vimentin at the identical location in osteosarcoma tissue specimens (Scale bar = 50 μm). (F) Correlation examination of MARCKS protein levels with VM density (r = −0.43, P = 0.0002) and Vimentin protein levels (r = −0.46, P < 0.0001) in osteosarcoma patients. (G−J) HOS cells transfected with *siNC* or *siMARCKS* (n = 3). (G) Representative images and quantification of tube formation (Scale bar = 200 μm). (H) Representative images and quantification of transendothelial invasion (Scale bar = 200 μm). (I) Immunofluorescence investigation of the expression of Vimentin, N-Cadherin, and VE-Cadherin (DAPI in blue; Vimentin in green; N-Cadherin and VE-Cadherin in red. Scale bar = 20 μm). (J) Western blot analysis indicating the expression of Vimentin, N-Cadherin, and VE-Cadherin. The data are presented as the mean ± SD. **P < 0.01, ***P < 0.001 *vs.* the mi-NC or siNC group. ns, not significant.
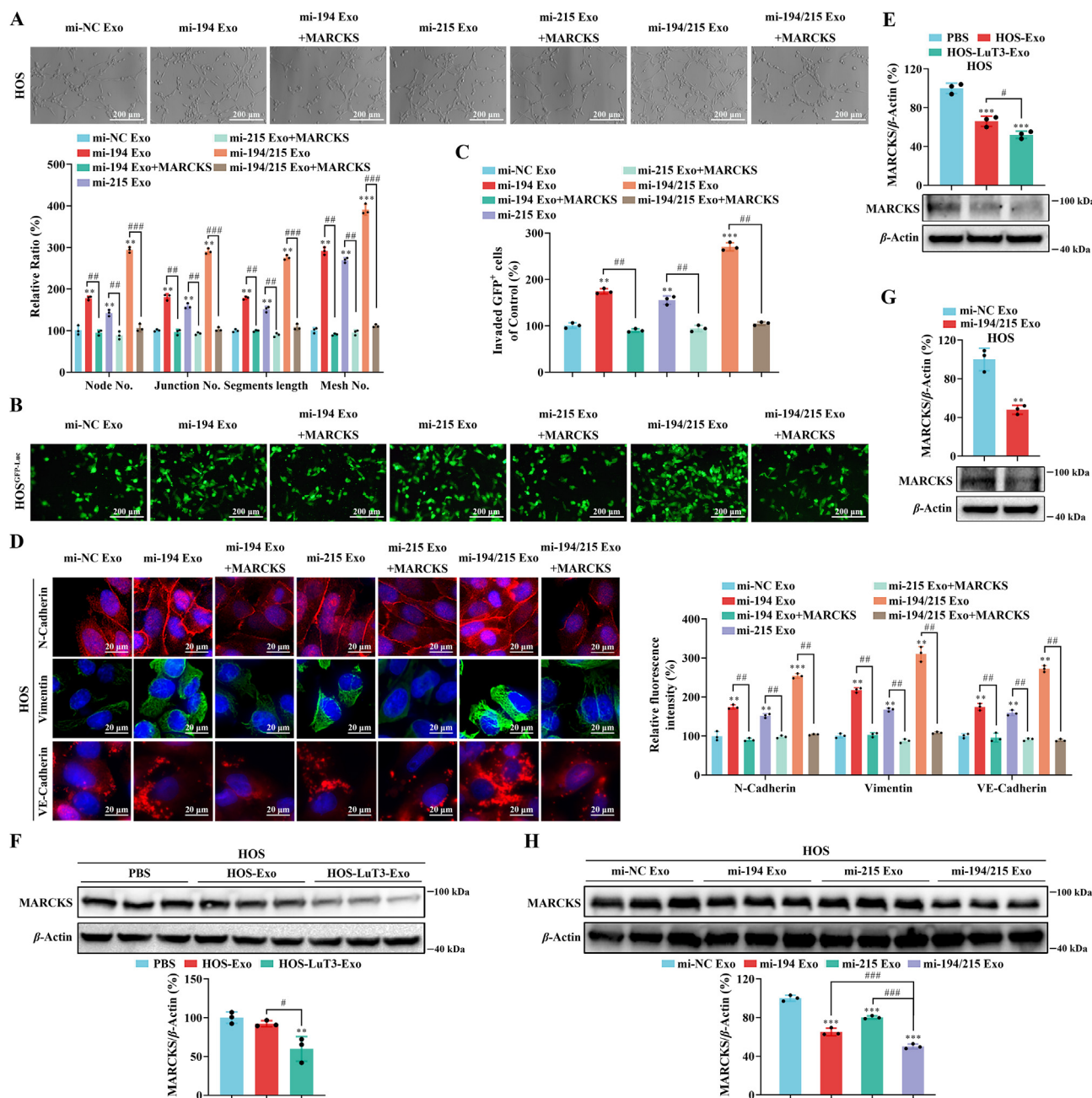
Figure 5 Elevation of MARCKS negates the metastatic potential augmentation of HOS cells by mi-194/215 Exo. (A−D) HOS cells were administered with miNC Exo, mi-194 Exo, mi-215 Exo, or mi-194/215 Exo and MARCKS ($n = 3$). (A) Representative images and quantification of tube formation (Scale bar = 200 μm). (B) Representative images illustrating transendothelial invasion (Scale bar = 200 μm). (C) Quantitative evaluation of GFP$^+$ HOS cells infiltrating through the HUVEC monolayer. (D) Immunofluorescence scrutiny of the expression of Vimentin, N-Cadherin, and VE-Cadherin (DAPI in blue; Vimentin in green; N-Cadherin and VE-Cadherin in red. Scale bar = 20 μm). (E) Western blot analysis of MARCKS protein expression levels in HOS cells administered with PBS, HOS-Exo, or HOS-LuT3-Exo ($n = 3$). (F) HOS cells implanted in NCG-HLA-A2.1 male mice tibia. Post 3 days, mice were intravenously administered with PBS, HOS-Exo, or HOS-LuT3-Exo every 3 days ($n = 6$). Western blot assessment of MARCKS protein expression levels in tumor tissues ($n = 3$). (G) Western blot examination of MARCKS protein expression levels in HOS cells treated with miNC Exo or mi-194/215 Exo ($n = 3$). (H) HOS cells implanted in NCG-HLA-A2.1 male mice tibia. Post 3 days, mice were intravenously administered with miNC Exo, mi-194 Exo, mi-215 Exo, or mi-194/215 Exo every 3 days ($n = 6$). Western blot analysis of MARCKS protein expression levels in tumor tissues ($n = 3$). The data are presented as the mean ± SD. $*P < 0.05$, $**P < 0.01$, $***P < 0.001$ *vs.* the mi-NC Exo or PBS group. $^\#P < 0.05$, $^{\#\#}P < 0.01$, $^{\#\#\#}P < 0.001$.

transcription factors such as Snail, Twist, or Slug. Fig. 6A shows that *siMARCKS* notably upregulated Slug expression in HOS cells, with Twist and Snail expression unaffected; substantiating this,

Western blot assays for both *in vivo* and *in vitro* experiments affirmed that HOS-LuT3-Exo greatly enhanced Slug protein expression (Fig. 6B and Supporting Information Fig. S14A).
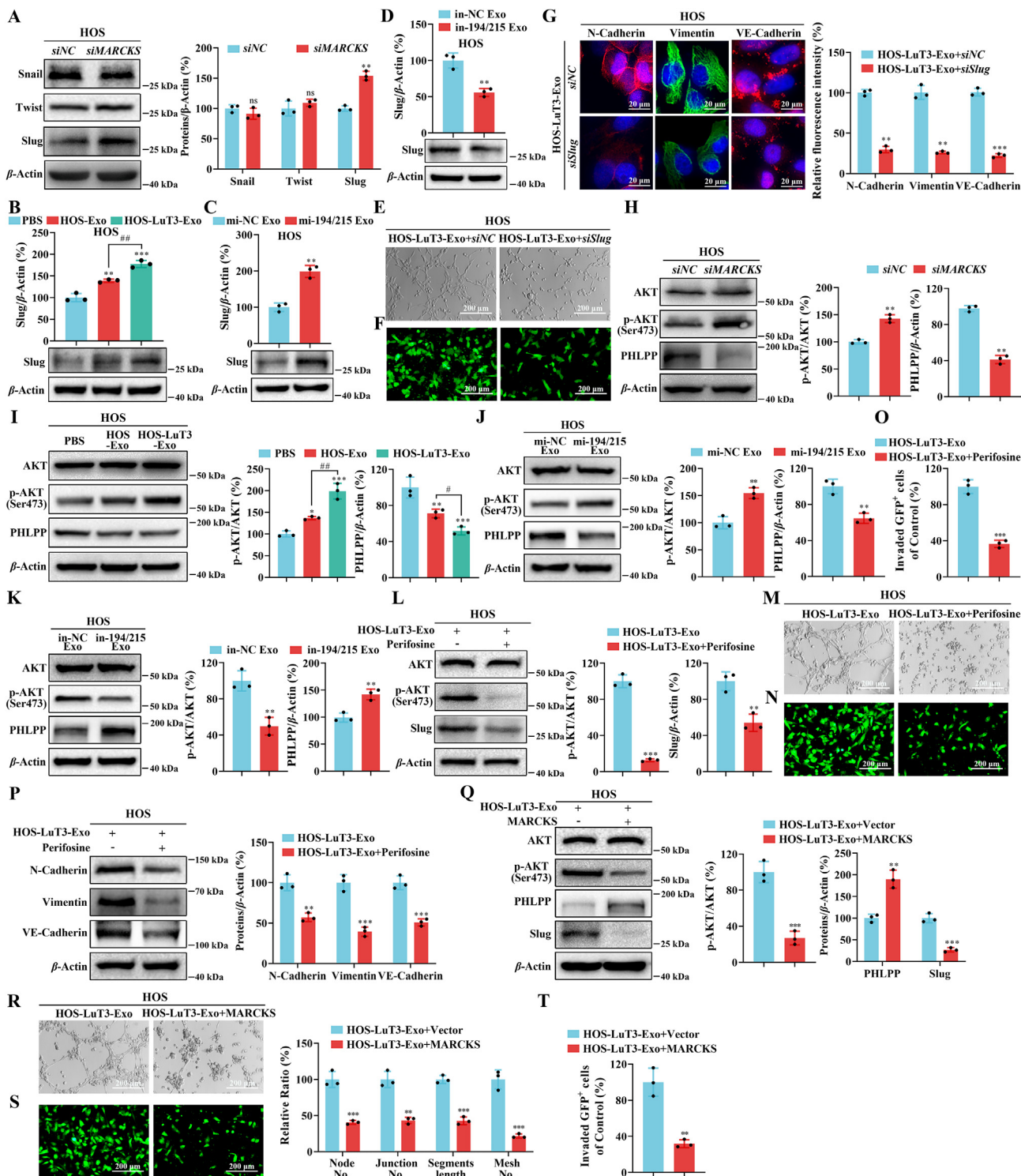
Figure 6 The exosomal miR-194/215 cluster/MARCKS axis propels EMT and VM formation *via* modulation of the PHLPP/p-AKT/Slug signaling pathway. (A) Western blot examination of Snail, Twist, and Slug protein expression levels in HOS cells subjected to *siNC* or *siMARCKS* transfection ($n = 3$). (B−D) Western blot analysis of Slug protein expression levels in HOS cells administered with (B) PBS, HOS-Exo or HOS-LuT3-Exo, (C) mi-NC Exo or mi-194/215 Exo, (D) in-NC Exo or in-194/215 Exo ($n = 3$). (E−G) HOS cells treated with HOS-LuT3-Exo in conjunction with *siNC* or *siSlug* ($n = 3$). (E) Representative images of tube formation (Scale bar = 200 μm). (F) Representative images illustrating transendothelial invasion (Scale bar = 200 μm). (G) Immunofluorescence evaluation of Vimentin, N-Cadherin, and VE-Cadherin expression (DAPI in blue; Vimentin in green; N-Cadherin and VE-Cadherin in red. Scale bar = 20 μm). (H−K) Western blot investigation of p-AKT(Ser473) and PHLPP protein expression levels in HOS cells subjected to transfection with (H) *siNC* or *siMARCKS*, (I) PBS, HOS-Exo or HOS-LuT3-Exo, (J) mi-NC Exo or mi-194/215 Exo, (K) in-NC Exo or in-194/215 Exo ($n = 3$). (L−P) HOS cells treated with HOS-LuT3-Exo and perifosine ($n = 3$). (L) Western blot evaluation of p-AKT(Ser473) and PHLPP protein expression levels.

Additionally, mi-194/215 Exo amplified Slug expression levels in HOS cells (Fig. 6C and Fig. S14B), and in-194/215 Exo led to a decrease in Slug expression (Fig. 6D). The role of Slug in osteosarcoma metastasis was further confirmed by using siRNA to knockdown Slug in HOS cells (Supporting Information Fig. S15A). Observations *via* microscopic imaging revealed that the inhibition of HOS-LuT3-Exo-induced tube formation and transendothelial invasion in HOS cells was due to Slug knockdown (Fig. 6E and F, Fig. S15B and S15C). Suppression of the protein expression of EMT and VM formation markers, which was otherwise promoted by HOS-LuT3-Exo, was also observed upon Slug knockdown (Fig. 6G).

Previous studies revealed that MARCKS is implicated in cancer cell migration *via* the AKT/Slug axis[38]. In this investigation, *MARCKS* silencing markedly augmented AKT phosphorylation at the Ser473 residue (Fig. 6H). PH domain and leucine-rich repeat protein phosphatase (PHLPP), a phosphatase that specifically dephosphorylates the hydrophobic motif (Ser473 in AKT), is known to inhibit tumor development[39]. Western blot analysis revealed that MARCKS silencing dramatically diminished PHLPP protein expression in HOS cells (Fig. 6H). Concurrently, an increase in p-AKT Ser473 expression and a decrease in PHLPP expression were observed in the HOS-LuT3-Exo group (Fig. 6I and Supporting Information Fig. S16A). In addition, mi-194/215 Exo increased the expression of p-AKT Ser473 in HOS cells and reduced PHLPP expression (Fig. 6J and Fig. S16B); in contrast, in-194/215 Exo decreased p-AKT Ser473 expression and increased PHLPP expression (Fig. 6K). These findings point toward the possibility that the exosomal miR-194/215 cluster/MARCKS axis promotes the lung metastasis of primary osteosarcoma through the PHLPP/p-AKT/Slug signaling pathway.

Finally, HOS cells were costimulated with the AKT inhibitor perifosine and HOS-LuT3-Exo. Perifosine counteracted the increased p-AKT Ser473 and Slug protein expression induced by HOS-LuT3-Exo (Fig. 6L). Microscopic imaging and Western blot analysis revealed the inhibitory effects of perifosine on tube formation, transendothelial invasion, and protein expression of EMT and VM formation markers, which were otherwise promoted by HOS-LuT3-Exo (Fig. 6M–P and Supporting Information Fig. S17). Subsequently, the impact of HOS-LuT3-Exo on HOS cells overexpressing MARCKS was examined. Western blot analyses indicated that MARCKS overexpression reversed p-AKT Ser473, PHLPP, and Slug protein expression in HOS cells treated with HOS-LuT3-Exo (Fig. 6Q). Investigations of tube formation and transendothelial invasion demonstrated that MARCKS overexpression curtailed the enhanced tube formation and transendothelial invasion capabilities of HOS cells induced by HOS-LuT3-Exo (Fig. 6R–T). Taken together, these observations suggest that the exosome-carried miR-194/215 cluster originating from pulmonary metastatic osteosarcoma lesions potentiates the lung metastasis of primary osteosarcoma by targeting MARCKS and modulating the PHLPP/p-AKT/Slug signaling pathway.

3.6. Therapeutic impact of bioengineered exosome mimetics (anta-194/215@Exo) targeting the miR-194/215 cluster in pulmonary–osteal axis transmission

Recognizing the role of the miR-194/215 cluster/MARCKS axis, propagated by pulmonary metastatic osteosarcoma exosomes, in promoting metastasis, a biomimetic design was implemented. This design utilized a CBSA-conjugated miR-194/215 cluster antagomir (anta-194/215) encapsulated by the membranes of the aforementioned exosomes (anta-194/215@Exo) (Fig. 7A). Surface zeta potential measurements confirmed that the charge of anta-194/215@Exo (-24.43 ± 0.70 mV) was akin to that of exosomal membranes (-26.53 ± 1.01 mV), unlike the positive charge (21.83 ± 1.01 mV) of the CBSA-anta-194/215 nano complex (Fig. 7B). These findings align with earlier reports, supporting the successful creation of biomimetic nanoparticles, wherein the membrane shell carries a charge resembling that of core–shell nanoparticles[40,41]. As determined using a Malvern Zetasizer Nano, the average particle size of anta-194/215@Exo was 229.13 ± 7.75 nm, slightly exceeding the typical sizes of exosome membrane vesicles[42], with a PDI of 0.113 ± 0.0076 (Fig. 7C). The morphology and size of anta-194/215@Exo were further confirmed by TEM (Fig. 7D). To ascertain the capability of anta-194/215@Exo to shield anta-194/215 from degradation, stability was evaluated in mouse serum and the presence of RNase. The results indicated substantial stability of the anta-194/215@Exo nanovesicles (Fig. 7E and F).

Further evaluation entailed assessing the delivery potential of the bioengineered exosome mimetics (anta-194/215@Exo), which was performed by loading anta-194-Cy5 and anta-215-FAM into the exosome membrane vesicles and exposing HOS cells to these vesicles. The presence of substantial FAM and Cy5 signals within the HOS cells substantiated the delivery potential of these engineered exosome mimetics for miR-194/215 cluster antagonists (Fig. 7G); this was further confirmed through the injection of anta-194/215-loaded PKH26-labeled exosome membrane vesicles into orthotopic osteosarcoma-bearing mice *via* the tail vein. The delivery of anta-194/215 to orthotopic osteosarcoma cells was evident, as demonstrated by enriched BLI signals in tibial tumors (Fig. 7H). The importance of biosafety in the application of nucleic acid drugs was assessed. Compared with PBS injection, anta-194/215@Exo injection into NCG mice resulted in no significant alterations in liver, kidney, and heart functions, and no toxicity was observed in histopathological studies of mouse tissues. The levels of alkaline phosphatase, alanine aminotransferase, aspartate aminotransferase, creatinine, urea, and creatine kinase remained within normal limits (Fig. 7I), with no detectable damage to the heart, liver, lungs, spleen, or kidneys (Fig. 7J). These results indicated a good biosafety profile of anta-194/215@Exo.

The impact of anta-194/215@Exo in inhibiting secondary lung metastasis from orthotopic osteosarcoma induced by pulmonary metastatic exosomes was evaluated. This was carried out by

(M) Representative images of tube formation (Scale bar = 200 μm). (N) Representative images illustrating transendothelial invasion (Scale bar = 200 μm). (O) Quantitative assessment of GFP$^+$ HOS cells infiltrating through the HUVEC monolayer. (P) Western blot investigation of Vimentin, N-Cadherin, and VE-Cadherin protein expression levels. (Q–T) HOS cells treated with HOS-LuT3-Exo and Vector or MARCKS ($n = 3$). (Q) Western blot evaluation of p-AKT(Ser473) and PHLPP protein expression levels. (R) Representative images and quantification of tube formation (Scale bar = 200 μm). (S) Representative images illustrating transendothelial invasion (Scale bar = 200 μm). (T) Quantitative evaluation of GFP$^+$ HOS cells infiltrating through the HUVEC monolayer. The data are presented as the mean $\pm$ SD. *$P < 0.05$, **$P < 0.01$, ***$P < 0.001$; ns, not significant *vs.* the *siNC*, PBS, mi-NC Exo, in-NC Exo, HOS-LuT3+*siNC*, HOS-LuT3-Exo or HOS-LuT3-Exo + Vector group. #$P < 0.05$, ##$P < 0.01$.
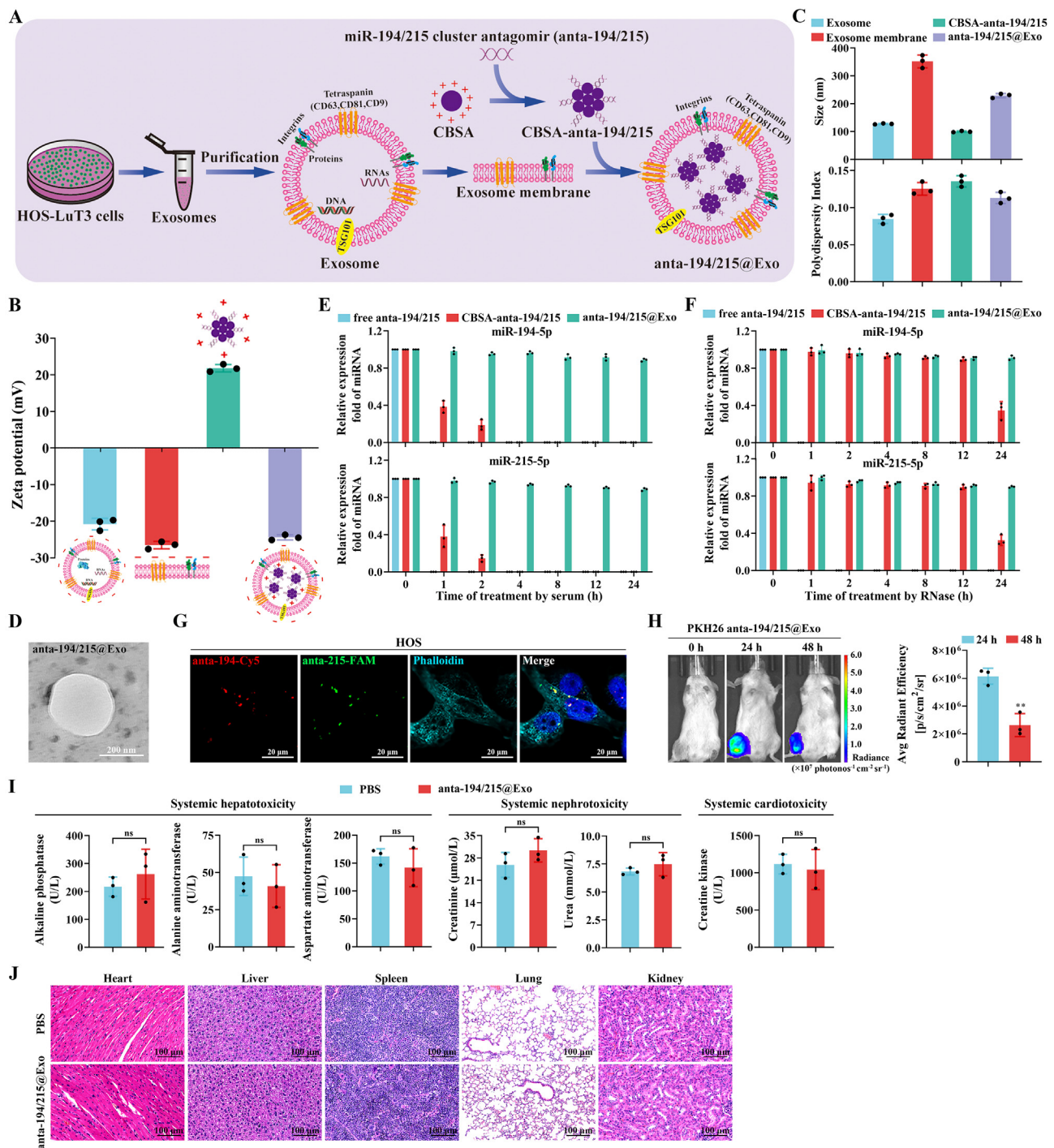
Figure 7 Physicochemical attributes and biosafety of bioengineered exosome mimics. (A) Schematic depiction of the preparation process of anta-miRNA@Exo nanoparticles. (B, C) Analysis of (B) zeta potential, (C) particle size, and PDI of anta-miRNA@Exo and its precursor ($n = 3$). (D) TEM image of anta-194/215@Exo nanoparticles (Scale bar = 200 nm). (E, F) Stability assessment of anta-194/215, CBSA-anta-194/215, and anta-194/215@Exo in the presence of (E) 50% mouse serum and (F) RNases, under incubation at 37 °C for specific durations ($n = 3$). (G) Fluorescence micrographs of HOS cells exposed to vesicles composed of HOS-LuT3 exosomal membrane-encapsulated CBSA-anta-194/215 (Cy5-labeled anta-194, FAM-labeled anta-215) over 24 h (Scale bar = 20 µm). (H) Representative images and quantification of BLI signals in mice after intravenous administration of PKH26-labeled anta-194/215@Exo in an orthotopic osteosarcoma mouse model ($n = 3$). (I, J) Post intravenous delivery of anta-194/215@Exo, (I) evaluation of systemic hepatotoxicity (alkaline phosphatase, alanine aminotransferase, and aspartate aminotransferase), nephrotoxicity (creatinine and urea), and cardiotoxicity (creatine kinase), in conjunction with (J) histopathological examination of the major organs in mice ($n = 3$). The data are presented as the mean ± SD. **$P < 0.01$ *vs.* the 24 h or PBS group. ns, not significant.

intravenously injecting HOS-bearing mice with HOS-LuT3-Exo and anta-194/215@Exo every three days (Fig. 8A). The outcomes, namely, tumor weight, Ki67 staining, CD31/PAS double staining, and mouse body weight, indicated that anta-194/215@Exo-treated mice exhibited a decreased bone tumor burden, fewer VM formations, and no discernible toxic side effects (Fig. 8B and C, Supporting Information Fig. S18A). Western blot analysis showed that anta-194/215@Exo downregulated the protein expression of tumor tissue N-Cadherin, Vimentin, and VE-Cadherin, which had been stimulated by HOS-LuT3-Exo (Fig. 8D and E). The reversal of orthotopic osteosarcoma lung metastasis promoted by HOS-LuT3-Exo was evident through Bouin's and H&E staining of lung tissues (Fig. 8F). Furthermore, tumor tissue Western blot results demonstrated the ability of anta-194/215@Exo to effectively upregulate the expression of MARCKS and PHLPP in tumors and downregulate the expression of Slug and p-AKT Ser473 (Fig. 8G and H, Fig. S18B). This suggested that anta-194/215@Exo inhibited orthotopic osteosarcoma lung metastasis by modulating the PHLPP/p-AKT/Slug signaling pathway *via* the exosomal miR-194/215 cluster/MARCKS axis. The 50-day survival curve for tumor-bearing mice revealed a survival rate of 66.67% (4/6) for the group treated with HOS-LuT3-Exo and anta-194/215@Exo; for the other groups, all mice died within 43 days of tumor inoculation (Fig. 8I). The findings underscore that the bioengineered exosome mimetics (anta-194/215@Exo) effectively inhibited lung−bone transmission of the miR-194/215 cluster, curtailing osteosarcoma progression and extending the survival duration of tumor-bearing mice. An in-depth exploration into its clinical efficacy is thus warranted.

4. Discussion

The present investigation uncovers the tumor-facilitating role of exosomes originating from lung metastases of osteosarcoma in the interplay between lung and bone. Intriguingly, exosomes from lung metastatic sites augment the metastatic propensity of osteosarcoma cells *via* the transfer of the miR-194/215 cluster, a finding that contributes to a comprehensive understanding of *in situ* osteosarcoma progression. Notably, the phenomenon of "self-seeding", where cancer cells from distant metastatic "seed" sites disseminate both locally and distally, eventually depositing back at their primary sites, is well-documented[43]. Exosomes derived from cancer cells have been identified recently as key vehicles of intercellular communication[44], with exosomes from distal metastases frequently demonstrating a superior seeding capability compared to that of their primary tumor counterparts[45]. Notably, exosomes from lung metastases deposit readily in bone tissues and are taken up by *in situ* osteosarcoma cells—a scenario potentially exemplifying a variation of "exosomal self-seeding". Furthermore, lung metastasis-derived exosomes are more abundantly present in orthotopic osteosarcoma than their progenitor exosomes, thereby paralleling the enhanced self-seeding effect observed in tumor cells[46]. Seeds elicit the progression of primary cancer by augmenting tumor growth, catalyzing angiogenesis, and mobilizing stromal cells. Consequently, in an endeavor to nullify the prospective tumorigenic effect triggered by "self-seeding" tumor cells within the lung−bone transmission, an animal model simulating *in situ* osteosarcoma was employed to investigate the potential impact of lung metastasis-derived exosomes on *in situ* osteosarcoma progression. Strikingly, *in situ* osteosarcoma cells exhibited a greater propensity to absorb exosomes secreted by lung metastatic osteosarcoma cells than to absorb those emanating from

parental osteosarcoma cells or Rab27a-knockdown lung metastatic osteosarcoma cells, as portrayed in Fig. 1A. This difference implies that the "self-seeding" induced by exosomes secreted by lung metastatic cells spurs the progression of *in situ* osteosarcoma.

On the genomic front, a miRNA cluster represents a collective of miRNA genes positioned in clusters on chromosomes. This investigation reveals that lung metastatic osteosarcoma-derived exosomes are laden with the miR-194/215 cluster. This cluster, upon transmission along the lung−bone transmission, incites the formation of EMT-induced VM, which in turn triggers the secondary metastasis of *in situ* osteosarcoma. The enhanced plasticity and motility associated with EMT-driven VM formation are regulated by the actin cytoskeleton and are orchestrated by MARCKS, a protein kinase C substrate integral to maintaining the dynamic equilibrium of the actin network[47]. AKT kinase is a crucial modulator in a multitude of biological processes, including EMT and VM formation. AKT can both directly and indirectly activate EMT and VM-related transcription factors[48], such as Snail, Slug, and Twist. These factors inhibit epithelial markers (such as E-cadherin), amplify mesenchymal markers (such as N-cadherin and Vimentin) and VM markers (VE-cadherin), and direct cytoskeletal remodeling to foster vascular mimicry. The phosphorylation of AKT at Ser473 bolsters its kinase activity, and PHLPP mediates the dephosphorylation of the hydrophobic motif (Ser473 in AKT1) of AKT[39]. Unveiled in the current investigation is the role of the exosomal miR-194/215 cluster in promoting EMT-induced VM formation *in situ* in osteosarcoma cells *via* the MARCKS/PHLPP/p-AKT/Slug pathway. This novel finding identifies the exosomal miR-194/215 cluster as a promising therapeutic target for treating osteosarcoma lung metastasis. Given the independent expression and unique roles of miR-194-5p and miR-215-5p across a range of malignant tumors—for instance, their ability to foster the migration and invasion of tumor cells in prostate and gastric cancer[49,50]—intervention with the exosomal miR-194/215 cluster might apply to various cancer types, paving the way for a new, promising approach in anticancer therapeutics.

Traditional therapies offer temporary protein modulation, but nucleic acid-based treatments promise lasting, possibly curative results through gene manipulation methods[51]. Gaining traction, these therapies target genetic blueprints but require strategies to ensure stability, target-specific delivery, and defense against degradation. Exosomes, naturally occurring nanocarriers, are being explored for delivering nucleic acid drugs, especially to tumors[52]. Given the ability of metastatic tumor exosomes to traverse the lung−primary site axis (Fig. 1), the strategic "hijacking" of these exosomes to intervene in the "lung−bone" transmission of the miR-194/215 cluster offers an innovative approach for the treatment of osteosarcoma metastasis. However, the high abundance of nucleic acids promoting metastasis inherently present in tumor exosomes represents a considerable threat to biosecurity (Fig. 2A−C)[53,54]. A potential solution lies in the construction of bioengineered exosome mimetics, achieved by enveloping nucleic acid-depleted exosome membranes around a nanoshell. In this study, we utilized CBSA to form nanoparticles with anta-miRNA *via* electrostatic interactions (CBSA-anta-miRNA), subsequently encapsulating these nanoparticles within the vesicles of lung metastatic foci exosomes (CBSA-anta-miRNA@Exo), presenting a straightforward and natural nanoscale drug delivery platform. These engineered exosomal vesicles not only shield anta-miRNAs from enzymatic degradation but also facilitate their delivery to primary osteosarcomas. Remarkably, anta-miRNA@Exo exhibits commendable biocompatibility and, by leveraging the role of the exosomal membrane in
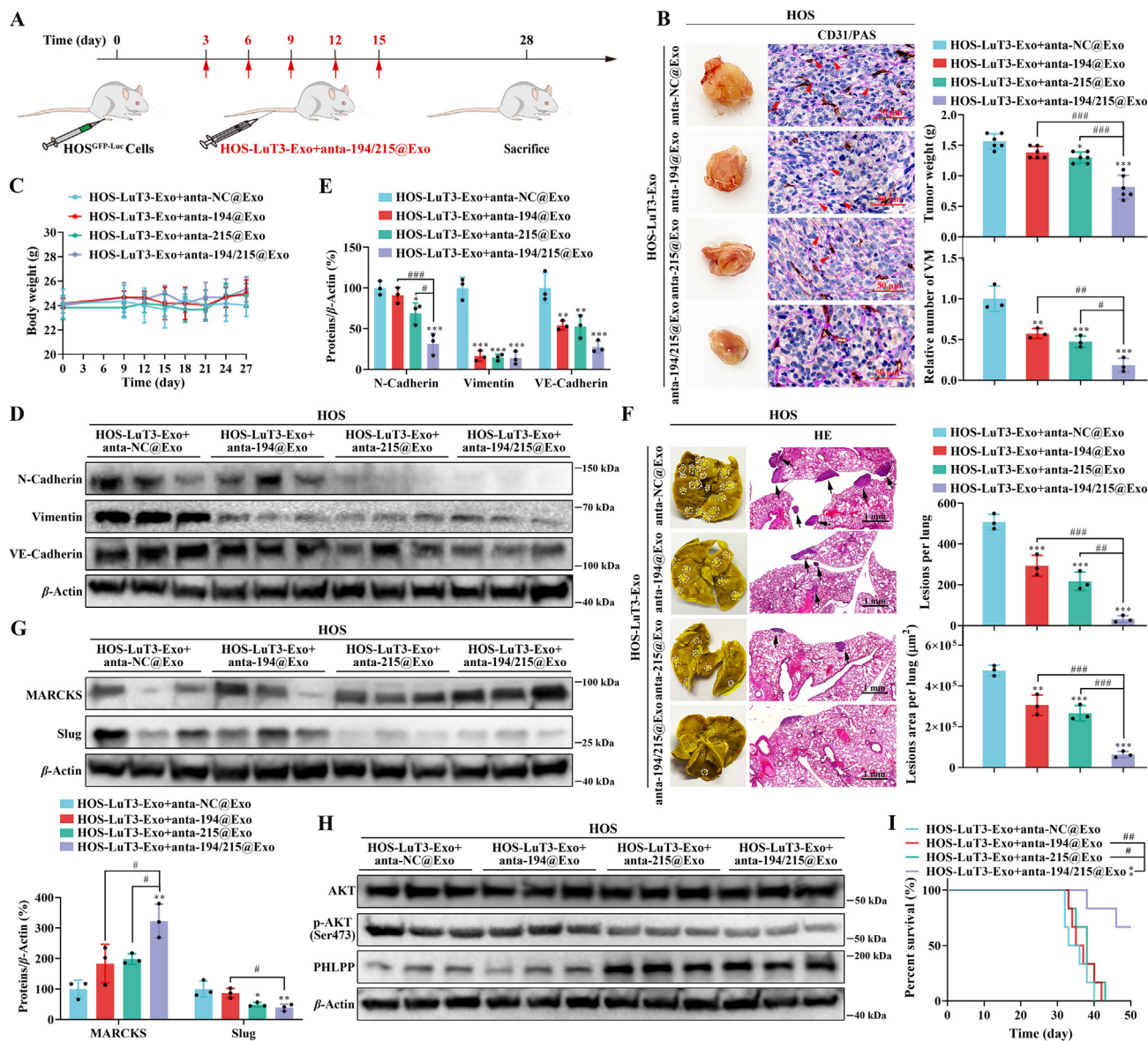
Figure 8 Therapeutic potential of bioengineered exosome mimetics (anta-194/215@Exo) targeting the miR-194/215 cluster. (A−H) Implantation of HOS cells into the tibia of NCG-HLA-A2.1 male mice, followed by intravenous injections of HOS-LuT3-Exo + anta-NC@Exo, HOS-LuT3-Exo + anta-194@Exo, HOS-LuT3-Exo + anta-215@Exo, or HOS-LuT3-Exo + anta-194/215@Exo every three days ($n = 6$). (A) Schematic representation of the orthotopic osteosarcoma animal model, inclusive of exosome treatment. (B) Depictive images of murine tumors and CD31/PAS staining in tumor tissue (Scale bar = 50 μm), supplemented by tumor weight quantification ($n = 6$) and relative quantification of VM ($n = 3$). (C) Average weight of diverse groups over 27 days. (D) and (E)Western blot evaluation of N-Cadherin, Vimentin, and VE-Cadherin protein expression levels in tumor tissues ($n = 3$). (F) Representative images of murine lungs and HE staining in lung tissue (Scale bar = 1 mm), in addition to quantification of lung metastatic foci ($n = 3$). (G) Western blot analysis of MARCKS and Slug protein expression levels in tumor tissue. (H) Western blot assessment of p-AKT (Ser473) and PHLPP protein expression levels in tumor tissue ($n = 3$). (I) Survival curves of mice from varied groups for 50 days. The data are presented as the mean ± SD. *$P < 0.05$, **$P < 0.01$, ***$P < 0.001$ vs. the HOS-LuT3-Exo + anta-NC@Exo group. #$P < 0.05$, ##$P < 0.01$, ###$P < 0.001$.

mediating lung−bone transmission, "hijacks" lung metastatic foci exosomes to accumulate in bones, leading to pronounced suppression of pulmonary metastasis. Furthermore, RNAi mediated by anta-194/215@Exo has been shown to downregulate the expression of the miR-194/215 cluster, inhibiting osteosarcoma progression and significantly prolonging the survival of tumor-bearing mice without manifesting overt toxicity. These outcomes underscore the potential of this "hijacking" treatment strategy employing core−shell nanoparticles enveloped in exosomal membranes as a

promising avenue for both cancer prophylaxis and therapeutic interventions.

Although engineered exosome mimetics show promise in mouse tumor models, their production is hindered by low tumor-derived exosome yields. Current culture methods are laborious and expensive, complicating large-scale exosome production for clinical use. 3D and bioreactor cultures, as highlighted by Patel et al.[55], increased yields, but they still fall short of clinical needs. Efforts to construct synthetic vesicles mimicking natural

exosomes are underway, using lipid bases and integrating native miRNAs and proteins. However, the complexity of natural exosomes presents technical challenges, with concerns over immunogenicity and safety[56]. Cell membranes, which are more readily obtainable and cost-effective than exosome membranes[57], offer potential. Given the similarities between exosomes and their source cells, bioengineering may enable the expression of key proteins for lung−bone transmission mediation on cell surfaces. While the roles of integrins in exosome organotropism are recognized—with specific integrins linked to lung and liver metastasis[45]—the exact integrins governing lung−bone transmission are unknown. Thus, a thorough protein analysis of HOS-LuT3 and HOS exosomes using tools such as CRISPR-Cas9 can identify the pivotal integrins in this transmission.

5. Conclusions

Our study underscores that exosomes from lung metastatic osteosarcoma transport the miR-194/215 cluster to primary osteosarcoma, promoting secondary metastasis *via* the MARCKS/PHLPP/p-AKT/Slug pathway and influencing VM through EMT. We introduce a hijacking therapeutic strategy harnessing this lung−bone transmission: bioengineered exosome mimetics (anta-194/215@Exo) built from CBSA-linked miR-194/215 antagonists and encased in exosomal membranes from pulmonary metastatic osteosarcoma. These mimetics target osteosarcoma, disrupting miR-194/215 transmission and hindering osteosarcoma progression.

Acknowledgments

Author contributions

Pei Yu: Conceptualization, Visualization, Data curation, Software, Formal Analysis, Writing-Original draft preparation. Yubao Han: Visualization, Investigation, Software, Formal Analysis. Lulu Meng, Yanyuan Tian, and Zhiwei Jin: Visualization, Investigation. Jun Luo, Chao Han, and Wenjun Xu: Writing-Reviewing and Editing. Lingyi Kong: Conceptualization, Supervision. Chao Zhang: Conceptualization, Supervision, Writing-Reviewing and Editing.

Conflicts of interest

The authors declare no conflicts of interest.

Appendix A. Supporting information

Supporting data to this article can be found online at https://doi.org/10.1016/j.apsb.2024.01.016.

References

1. Isakoff MS, Bielack SS, Meltzer P, Gorlick R. Osteosarcoma: current treatment and a collaborative pathway to success. *J Clin Oncol* 2015;**33**:3029−35.
2. Wang J, Ni J, Song D, Ding M, Huang J, Li W, et al. MAT1 facilitates the lung metastasis of osteosarcoma through upregulation of AKT1 expression. *Life Sci* 2019;**234**:116771.
3. Kansara M, Teng MW, Smyth MJ, Thomas DM. Translational biology of osteosarcoma. *Nat Rev Cancer* 2014;**14**:722−35.
4. Zhang W, Zhao JM, Lin J, Hu CZ, Zhang WB, Yang WL, et al. Adaptive fibrogenic reprogramming of osteosarcoma stem cells promotes metastatic growth. *Cell Rep* 2018;**24**:1266−1277.e5.
5. Shen T, Liu JL, Wang CY, Rixiati Y, Li S, Cai LD, et al. Targeting Erbin in B cells for therapy of lung metastasis of colorectal cancer. *Signal Transduct Targeted Ther* 2021;**6**:115.
6. Yan Y, Du C, Duan X, Yao X, Wan J, Jiang Z, et al. Inhibiting collagen I production and tumor cell colonization in the lung *via* miR-29a-3p loading of exosome-/liposome-based nanovesicles. *Acta Pharm Sin B* 2022;**12**:939−51.
7. Kovar H. Selective enhancer changes in osteosarcoma lung metastasis. *Nat Med* 2018;**24**:126−7.
8. Lee YC, Kurtova AV, Xiao J, Nikolos F, Hayashi K, Tramel Z, et al. Collagen-rich airway smooth muscle cells are a metastatic niche for tumor colonization in the lung. *Nat Commun* 2019;**10**:2131.
9. Chao CC, Lee CW, Chang TM, Chen PC, Liu JF. CXCL1/CXCR2 paracrine axis contributes to lung metastasis in osteosarcoma. *Cancers* 2020;**12**:459.
10. Zeng C, Zhong L, Liu W, Zhang Y, Yu X, Wang X, et al. Targeting the lysosomal degradation of Rab22a-NeoF1 fusion protein for osteosarcoma lung metastasis. *Adv Sci* 2023;**10**:e2205483.
11. Zhong L, Liao D, Li J, Liu W, Wang J, Zeng C, et al. Rab22a-NeoF1 fusion protein promotes osteosarcoma lung metastasis through its secretion into exosomes. *Signal Transduct Targeted Ther* 2021;**6**:59.
12. Dai J, Su Y, Zhong S, Cong L, Liu B, Yang J, et al. Exosomes: key players in cancer and potential therapeutic strategy. *Signal Transduct Targeted Ther* 2020;**5**:145.
13. Liu W, Wang B, Duan A, Shen K, Zhang Q, Tang X, et al. Exosomal transfer of miR-769-5p promotes osteosarcoma proliferation and metastasis by targeting DUSP16. *Cancer Cell Int* 2021;**21**:541.
14. Chen C, Mao X, Cheng C, Jiao Y, Zhou Y, Ren T, et al. miR-135a reduces osteosarcoma pulmonary metastasis by targeting both BMI1 and KLF4. *Front Oncol* 2021;**11**:620295.
15. Pidikova P, Reis R, Herichova I. miRNA clusters with down-regulated expression in human colorectal cancer and their regulation. *Int J Mol Sci* 2020;**21**:4633.
16. Xie B, Ding Q, Han H, Wu D. miRCancer: a microRNA-cancer association database constructed by text mining on literature. *Bioinformatics* 2013;**29**:638−44.
17. Aderem A. The marcks brothers—a family of protein-kinase-C substrates. *Cell* 1992;**71**:713−6.
18. Chen XY, Rotenberg SA. PhosphoMARCKS drives motility of mouse melanoma cells. *Cell Signal* 2010;**22**:1097−103.
19. Micallef J, Taccone M, Mukherjee J, Croul S, Busby J, Moran MF, et al. Epidermal growth factor receptor variant III-induced glioma invasion is mediated through myristoylated alanine-rich protein kinase C substrate overexpression. *Cancer Res* 2009;**69**:7548−56.
20. Jarboe JS, Anderson JC, Duarte CW, Mehta T, Nowsheen S, Hicks PH, et al. MARCKS regulates growth and radiation sensitivity and is a novel prognostic factor for glioma. *Clin Cancer Res* 2012;**18**:3030−41.
21. Yokoyama Y, Ito T, Hanson V, Schwartz GK, Aderem AA, Holland JF, et al. PMA-induced reduction in invasiveness is associated with hyperphosphorylation of MARCKS and talin in invasive bladder cancer cells. *Int J Cancer* 1998;**75**:774−9.
22. Hua Y, Han A, Yu T, Hou Y, Ding Y, Nie H. Small extracellular vesicles containing miR-34c derived from bone marrow mesenchymal

stem cells regulates epithelial sodium channel *via* targeting MARCKS. *Int J Mol Sci* 2022;**23**:5196.

23. Keklikoglou I, Cianciaruso C, Guc E, Squadrito ML, Spring LM, Tazzyman S, et al. Chemotherapy elicits pro-metastatic extracellular vesicles in breast cancer models. *Nat Cell Biol* 2019;**21**:190−202.

24. Luan W, Ding Y, Xi H, Ruan H, Lu F, Ma S, et al. Exosomal miR-106b-5p derived from melanoma cell promotes primary melanocytes epithelial−mesenchymal transition through targeting EphA4. *J Exp Clin Cancer Res* 2021;**40**:107.

25. Armacki M, Polaschek S, Waldenmaier M, Morawe M, Ruhland C, Schmid R, et al. Protein kinase D1, reduced in human pancreatic tumors, increases secretion of small extracellular vesicles from cancer cells that promote metastasis to lung in mice. *Gastroenterology* 2020; **159**:1019−1035.e22.

26. Pena JT, Sohn-Lee C, Rouhanifard SH, Ludwig J, Hafner M, Mihailovic A, et al. miRNA *in situ* hybridization in formaldehyde and EDC-fixed tissues. *Nat Methods* 2009;**6**:139−41.

27. Pei W, Li X, Bi R, Zhang X, Zhong M, Yang H, et al. Exosome membrane-modified M2 macrophages targeted nanomedicine: treatment for allergic asthma. *J Control Release* 2021;**338**:253−67.

28. García-Heredia JM, Otero-Albiol D, Pérez M, Pérez-Castejón E, Muñoz-Galván S, Carnero A. Breast tumor cells promotes the horizontal propagation of EMT, stemness, and metastasis by transferring the MAP17 protein between subsets of neoplastic cells. *Oncogenesis* 2020;**9**:96.

29. Ren K, Ni Y, Li X, Wang C, Chang Q, Li Y, et al. Expression profiling of long noncoding RNAs associated with vasculogenic mimicry in osteosarcoma. *J Cell Biochem* 2019;**120**:12473−88.

30. Sun T, Zhao N, Zhao XL, Gu Q, Zhang SW, Che N, et al. Expression and functional significance of Twist1 in hepatocellular carcinoma: its role in vasculogenic mimicry. *Hepatology* 2010;**51**:545−56.

31. Li W, Zong S, Shi Q, Li H, Xu J, Hou F. Hypoxia-induced vasculogenic mimicry formation in human colorectal cancer cells: involvement of HIF-1α, Claudin-4, and E-cadherin and Vimentin. *Sci Rep* 2016;**6**:37534.

32. Zhou W, Fong MY, Min Y, Somlo G, Liu L, Palomares MR, et al. Cancer-secreted miR-105 destroys vascular endothelial barriers to promote metastasis. *Cancer Cell* 2014;**25**:501−15.

33. Yu P, Zhu X, Zhu JL, Han YB, Zhang H, Zhou X, et al. The Chk2−PKM2 axis promotes metabolic control of vasculogenic mimicry formation in p53-mutated triple-negative breast cancer. *Oncogene* 2021;**40**:5262−74.

34. Wei X, Chen Y, Jiang X, Peng M, Liu Y, Mo Y, et al. Mechanisms of vasculogenic mimicry in hypoxic tumor microenvironments. *Mol Cancer* 2021;**20**:7.

35. Valadi H, Ekstrom K, Bossios A, Sjostrand M, Lee JJ, Lotvall JO. Exosome-mediated transfer of mRNAs and microRNAs is a novel mechanism of genetic exchange between cells. *Nat Cell Biol* 2007;**9**:654−9.

36. Hu T, He N, Yang Y, Yin C, Sang N, Yang Q. DEC2 expression is positively correlated with HIF-1 activation and the invasiveness of human osteosarcomas. *J Exp Clin Cancer Res* 2015;**34**:22.

37. Osaki M, Takeshita F, Sugimoto Y, Kosaka N, Yamamoto Y, Yoshioka Y, et al. MicroRNA-143 regulates human osteosarcoma metastasis by regulating matrix metalloprotease-13 expression. *Mol Ther* 2011;**19**:1123−30.

38. Chen CH, Thai P, Yoneda K, Adler KB, Yang PC, Wu R. A peptide that inhibits function of myristoylated alanine-rich C kinase substrate

39. Gao T, Furnari F, Newton AC. PHLPP: a phosphatase that directly dephosphorylates Akt, promotes apoptosis, and suppresses tumor growth. *Mol Cell* 2005;**18**:13−24.

40. Dehaini D, Wei X, Fang RH, Masson S, Angsantikul P, Luk BT, et al. Erythrocyte-platelet hybrid membrane coating for enhanced nanoparticle functionalization. *Adv Mater* 2017;**29**: 10.1002/adma.201606209.

41. Hu CM, Fang RH, Wang KC, Luk BT, Thamphiwatana S, Dehaini D, et al. Nanoparticle biointerfacing by platelet membrane cloaking. *Nature* 2015;**526**:118−21.

42. Zhao L, Gu C, Gan Y, Shao L, Chen H, Zhu H. Exosome-mediated siRNA delivery to suppress postoperative breast cancer metastasis. *J Control Release* 2020;**318**:1−15.

43. Comen E, Norton L, Massagué J. Clinical implications of cancer self-seeding. *Nat Rev Clin Oncol* 2011;**8**:369−77.

44. Dioufa N, Clark AM, Ma B, Beckwitt CH, Wells A. Bi-directional exosome-driven intercommunication between the hepatic niche and cancer cells. *Mol Cancer* 2017;**16**:172.

45. Hoshino A, Costa-Silva B, Shen TL, Rodrigues G, Hashimoto A, Tesic Mark M, et al. Tumour exosome integrins determine organotropic metastasis. *Nature* 2015;**527**:329−35.

46. Kim MY, Oskarsson T, Acharyya S, Nguyen DX, Zhang XH, Norton L, et al. Tumor self-seeding by circulating cancer cells. *Cell* 2009;**139**:1315−26.

47. Yamaguchi H, Condeelis J. Regulation of the actin cytoskeleton in cancer cell migration and invasion. *Biochim Biophys Acta* 2007;**1773**:642−52.

48. Li F, Sun H, Yu Y, Che N, Han J, Cheng R, et al. RIPK1-dependent necroptosis promotes vasculogenic mimicry formation *via* eIF4E in triple-negative breast cancer. *Cell Death Dis* 2023;**14**:335.

49. Das R, Gregory PA, Fernandes RC, Denis I, Wang Q, Townley SL, et al. MicroRNA-194 promotes prostate cancer metastasis by inhibiting SOCS2. *Cancer Res* 2017;**77**:1021−34.

50. Zang Y, Wang T, Pan J, Gao F. miR-215 promotes cell migration and invasion of gastric cancer cell lines by targeting FOXO1. *Neoplasma* 2017;**64**:579−87.

51. Kulkarni JA, Witzigmann D, Thomson SB, Chen S, Leavitt BR, Cullis PR, et al. The current landscape of nucleic acid therapeutics. *Nat Nanotechnol* 2021;**16**:630−43.

52. Tian Y, Li S, Song J, Ji T, Zhu M, Anderson GJ, et al. A doxorubicin delivery platform using engineered natural membrane vesicle exosomes for targeted tumor therapy. *Biomaterials* 2014;**35**:2383−90.

53. Tan S, Xia L, Yi P, Han Y, Tang L, Pan Q, et al. Exosomal miRNAs in tumor microenvironment. *J Exp Clin Cancer Res* 2020;**39**:67.

54. Tuo B, Chen Z, Dang Q, Chen C, Zhang H, Hu S, et al. Roles of exosomal circRNAs in tumour immunity and cancer progression. *Cell Death Dis* 2022;**13**:539.

55. Patel DB, Santoro M, Born LJ, Fisher JP, Jay SM. Towards rationally designed biomanufacturing of therapeutic extracellular vesicles: impact of the bioproduction microenvironment. *Biotechnol Adv* 2018; **36**:2051−9.

56. Santos G. No place like home. *Science* 2020;**368**:1150.

57. Han S, Xue L, Wei Y, Yong T, Jia W, Qi Y, et al. Bone lesion-derived extracellular vesicles fuel prometastatic cascades in hepatocellular carcinoma by transferring ALKBH5-targeting miR-3190-5p. *Adv Sci* 2023;**10**:e2207080.